

Analysis Note of the Experiment

Measurement of diffractive Central Exclusive Production of h^+h^- pairs ($h = \pi, K, p$) in proton-proton collisions at $\sqrt{s} = 200$ GeV with forward proton reconstruction in Roman Pot detectors

Leszek Adamczyk , Łukasz Fulek , Mariusz Przybycień , and Rafał Sikora

AGH University of Science and Technology, FPACS, Kraków, Poland

April 9, 2019

Abstract

In this note we present analysis of diffractive Central Exclusive Production using 2015 data from proton-proton collisions at $\sqrt{s} = 200$ GeV. This dataset was collected with newly installed Roman Pot detectors in Phase II* configuration which ensured efficient triggering and measuring diffractively scattered protons. We describe intermediate stages of analysis involving choice of selection cuts, comparison of data with Monte Carlo models folded into detector acceptance, and study of systematic uncertainties specific to the analysis. Finally, we show the physics outcome of the analysis. Parts of the analysis which are of more technical nature (calculation of efficiencies, derivation of corrections to efficiencies, adjustment of the STAR simulation, systematic uncertainty of efficiencies) are described in a supplementary analysis note [1].

ver. 0.9

Contents

List of contributions	4
Change log	4
1 Introduction	5
1.1 Central Exclusive Production	5
1.2 Double IPomeron Exchange	5
1.3 Physics motivation for the measurement	6
1.3.1 DIPE differential cross-sections, mass spectrum	6
1.3.2 Absorption effects	6
1.3.3 Size of interaction region	6
2 Data set	7
2.1 Trigger	7
2.2 Reconstruction software	8
2.3 Data format	8
3 Event selection	9
3.1 List of cuts	9
3.2 Description of cuts	10
3.2.1 (C1,C2) Primary vertex and its z -position	10
3.2.2 (C3) TPC tracks	10
3.2.3 (C4) RP tracks	14
3.2.4 (C5) TPC-RP z -vertex matching	14
3.2.5 (C6) BBC-large signal veto	14
3.2.6 (C7) TOF clusters limit	16
3.2.7 (C8) Exclusivity cut (missing p_T cut)	17
3.2.8 (C9) Particle identification	17
3.3 Working point for cuts C6, C7 and C8	19
3.4 Signal per integrated luminosity	19
3.5 Cut flow	19
4 Corrections	21
4.1 Method of corrections application	21
4.2 Efficiencies and acceptances	21
4.2.1 Trigger efficiency	21
4.2.1.1 Online veto (BBC-small and ZDC veto)	21
4.2.1.2 RP triggering efficiency	22
4.2.1.3 Up and Down RP combination veto	22
4.2.2 Cuts efficiency	22
4.2.2.1 TPC z -vertex cut (C2)	22
4.2.2.2 TPC-RP z -vertex matching (C5)	22
4.2.2.3 Primary vertices limit (C1), BBC-large veto (C6) and TOF clusters limit (C7)	22
4.2.2.4 Missing p_T cut (C8)	22
4.2.2.5 Particle identification (C9)	22
4.2.3 RP track acceptance and reconstruction efficiency	22
4.2.4 TPC vertex reconstruction efficiency	24
4.3 Particle energy loss	24
4.4 Background subtraction	24

5 Backgrounds	25
5.1 Sources of background	25
5.1.1 Non-exclusive background	25
5.1.2 Exclusive background (particle misidentification)	25
5.2 Relative normalization of background and signal	26
6 Systematic errors	27
7 Physics results	28
Appendix A BBC response	33
Appendix B Formulation of total RP efficiency	42
Appendix C Reconstruction of m_{TOF}^2	44
Appendix D RP efficiency	45
D.1 RP track acceptance, reconstruction and selection efficiency	45
D.2 RP trigger veto probability related to dead material	51
List of Figures	58
List of Tables	58
References	60

List of contributions

Leszek Adamczyk	Analysis coordination/supervision, production of picoDST, production of embedded MC samples
Lukasz Fulek	Analysis support
Mariusz Przybycień	Analysis supervision
Rafał Sikora*	Main analyzer

* - contact editor

Change log

?? Apr 2019 ver. 1.0 Initial revision

1. Introduction

1.1 Central Exclusive Production

The Central Exclusive Production (CEP) takes place when interacting particles form a state in the mid-rapidity region (“central production”) whose all constituents/decay products are measured in the detector (“exclusive”). The initial state particles can either dissociate, excite or stay intact. The latter case of CEP in proton-proton collisions can be written as

$$p + p \rightarrow p + X + p \quad (1.1)$$

and depicted as in Fig. 1.1. Mass and rapidity of state X is given by

$$M_X = \sqrt{s(\xi_1 \xi_2 \sin^2(\alpha/2) - (1 - \xi_1 - \xi_2) \cos^2(\alpha/2))} \stackrel{\alpha=\pi}{=} \sqrt{s\xi_1 \xi_2}, \quad (1.2)$$

where α is angle between scattered protons and $\xi = (p_0 - p)/p_0$ is the fractional momentum loss of proton.

1.2 Double IPomeron Exchange

Reaction from Eq. (1.1) can exhibit purely electromagnetic ($\gamma\gamma$ interaction), mixed ($\gamma\mathcal{O}$ interaction) or purely strong nature ($\mathcal{O}\mathcal{O}$ interaction). The last type is dominant at RHIC energies. It is characterized by the lack of hard scale (if protons are scattered at small angles), therefore perturbative QCD cannot be applied and Regge theory [2] is used instead. An object \mathcal{O} does not have unequivocal QCD representation - in Regge formalism it is the so-called “trajectory” (IReggeon, IR). IReggeon with quantum numbers of vacuum is called ”IPomeron“ (IP) and IP-IP reaction (Fig. 1.2) is called ”Double IPomeron Exchange“.

Processes involving IPomeron exchange are referred as diffraction due to cross-section in scattering angle resembling similar shape to intensity pattern of diffracted light. For low values of Mandelstam t (small scattering angles) cross-section takes exponential form

$$\frac{d\sigma}{d|t|} \propto e^{-B|t|}, \quad (1.4)$$

where the slope parameter B reflects the size of target at which IPomerons scatter.

Diffractive events have specific property of the ”rapidity gap“ which is an angular region free of hadrons. In DIPPE two such gaps are present, marked in Fig. 1.1 as $\Delta\eta_1$ and $\Delta\eta_2$.

DIPPE is a spin-parity filter - the fact that scattered particles have all quantum numbers unchanged after the interaction, production of central states satisfying Eq. (1.5) is enhanced

$$I^G J^{PC} = 0^+ \text{even}^{++}. \quad (1.5)$$

The lowest order QCD picture of the IPomeron is a pair of oppositely colored gluons (colour singlet). This fact makes the DIPPE recognized as the gluon-rich environment process in which bound states of gluons (”glueballs“) or hybrid mesons could be preferably produced.

For detailed introduction to the topic of diffraction see Refs. [3, 4].

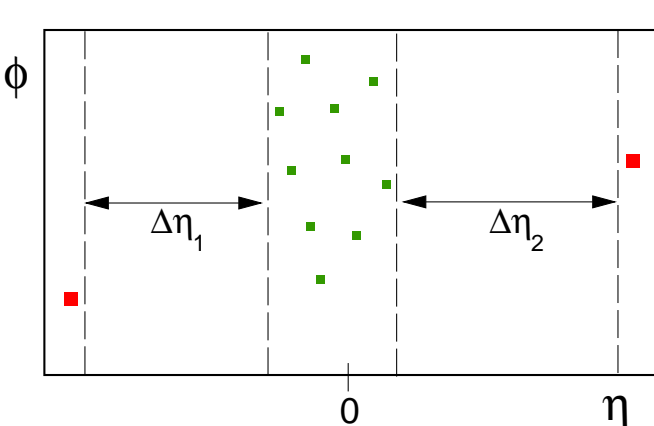


Figure 1.1: CEP represented in $\eta\phi$ space.

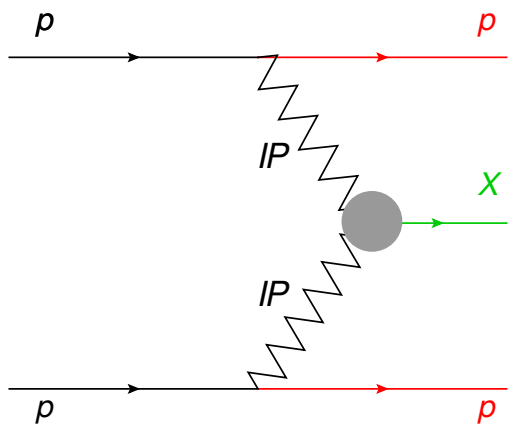


Figure 1.2: Diagram of DIPPE process.

1.3 Physics motivation for the measurement

STAR collected in 2015 large dataset dedicated for measurement of the Central Diffraction (DIPE in particular). Since that year the experiment was enriched with Roman Pot Phase II* subsystem and thus gained possibility of detection of forward protons. It enabled studies of properties of the central state with respect to observables related to exchanged IPomerons. No such measurement was performed before at that high c.m.s. energy ($\sqrt{s} = 200$ GeV, contamination from Reggeon exchanges is small) which makes it particularly attractive. A brief list of physics issues that can be covered with the study described in this note is briefly introduced below.

1.3.1 DIPE differential cross-sections, mass spectrum

As stated in Sec. 1.2 DIPE is a soft process whose theoretical description is done mainly using phenomenological tools, thus measurement of differential cross-sections is needed to verify various production models.

The main focus is put on the simplest state (and most numerous) produced in DIPE, namely a pair of oppositely charged pions, $\pi^+\pi^-$. It can be formed either in a non-resonant or resonant mechanism. In the first case the $\pi^+\pi^-$ continuum is formed by the exchange of the off-shell pion between IPomerons. Currently there are two models of this reaction on the market [5, 6], [7]. In the second case the IPomerons directly couple into resonance (e.g. $f_2(1270)$), which then decays to $\pi^+\pi^-$. Attempts to calculate cross-section for this production mechanism are presented in Ref. [6] and [8].

Understanding of the mass spectrum in $\pi^+\pi^-$ channel is important to learn about relative contribution from continuum and resonant production, as well as relative production of resonances. Recognition of resonant states may indicate candidates for low-mass glueballs of $J^{PC} = 0^{++}$, however presence of underlaying scalar $q\bar{q}$ states makes this task challenging.

Other channels, like K^+K^- , are also of great interest. Comparison of the cross-sections for production of $\pi^+\pi^-$ and K^+K^- gives information about strength of the IPomeron coupling to different quark flavors. Also, structures in $d\sigma/dm$ can be easier attributed to resonances by measuring more than one channel and known branching ratios thereof.

Detection of intact protons scattered at very small angle with respect to the beamline enables determination of the reaction plane which makes the Partial Wave Analysis (PWA) possible. It also allows to look at the cross-sections more differentially, especially with respect to properties of exchanged IPomerons, like carried squared four-momentum t , azimuthal separation of IPomerons in the transverse plane $\Delta\varphi$ or relative momentum of IPomerons Δp_T . The last quantity was proposed to distinguish pure $q\bar{q}$ states from these with gluonic content [9].

1.3.2 Absorption effects

One can imagine in diagram in Fig. 1.2 additional soft lines e.g. between protons in the initial state or one of IPomerons and final state proton. These so-called rescattering effects (or absorption effects) lead to production of hadrons other than these belonging to central state X hence the diffractive signature of an event in form of rapidity gap is no longer present. Measurement of the probability that the state X will remain exclusive and forward protons will remain intact, in other words the rapidity gap survival probability S^2 , would be valuable ingredient for development of absorption models.

1.3.3 Size of interaction region

From the measurement of protons in Roman Pots one is able to reconstruct squared four-momenta transferred in proton-IPomeron vertices and determine the differential cross-section $d\sigma/d|t|$. Fit of exponent allows to extract the slope parameter B , which may depend on the IPomeron-IPomeron c.m.s. energy, or in other words on the mass of diffractive system X . Knowledge on the slope parameter gives insight to the form factor of the object at which IPomeron scatters.

2. Data set

2.1 Trigger

The main trigger designed for studies of Central Diffraction in run 15 was RP_CPT2. It was formed of the following conditions combined by logical AND ($\&\&$):

1. **(ET $\&\&$!IT) || (!ET $\&\&$ IT)** = signal in at least one RP on each side of the STAR central detector
- to ensure presence of two forward-scattered protons; a veto was imposed on simultaneous signal in RPs above and below the beamline, which might have originated either from proton dissociation, or pile-up event, or beam halo proton etc.,
2. **!BBC-E $\&\&$!BBCW $\&\&$!ZDCE $\&\&$!ZDCW** = veto on any signal in small BBC tiles or ZDCs on any side of STAR central detector - such requirement is in accordance with the double-gap topology of CEP events, it mostly filtered out CEP events with parallel pile-up event(s),
3. **TOF ≥ 2** = at least 2 hits in TOF - aim of this condition was to ensure activity in the mid-rapidity; since the lowest multiplicity allowed in CEP is 2, that was the lower threshold of L0 TOF multiplicity.

This trigger was running with an average prescale of 5 and average DAQ rate of 250 Hz, which allowed to collect in total about 560 M events corresponding to 16.5 pb^{-1} of integrated luminosity. More information about number of events per run, rates etc. can be found under link provided in Ref. [10], which contains selected data from STAR run log [11]. Luminosity data used in this analysis comes from Ref. [12].

All RP triggers which were intended for usage in diffractive physics analyses or efficiency studies are listed in Tab. 2.1. Components used in definitions of these triggers are outlined in Fig. 2.1. Detailed explanation of all trigger bits can be found in Refs. [13, 14]. Explanation of naming convention in Roman Pot system can be found in Ref. [15].

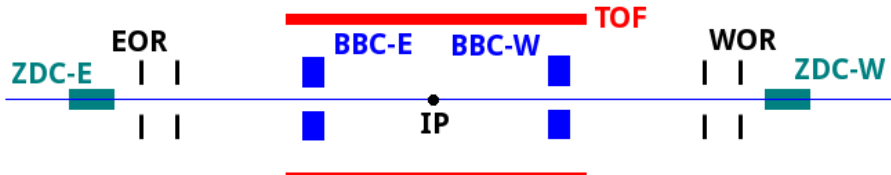


Figure 2.1: Sketch of the trigger components used in definitions of diffractive triggers in run 15.

Trigger name	Definition	Events [M]	Comment
RP_CPT	EOR $\&\&$ WOR	73.3	Loose trigger (mostly elastic events) designed for monitoring/trigger efficiency study
RP_CPT	EOR $\&\&$ WOR $\&\&$!BBC-E $\&\&$!BBCW $\&\&$!ZDCE $\&\&$!ZDCW $\&\&$ TOF ≥ 1	38.9	Intended to be main CEP trigger (later switched to RP_CPT2 due to large prescale)
RP_CPT2	(ET $\&\&$!IT) (!ET $\&\&$ IT) $\&\&$!BBC-E $\&\&$!BBCW $\&\&$!ZDCE $\&\&$!ZDCW $\&\&$ TOF ≥ 2	556.5	Main CEP trigger Note: On Apr 14 added upper TOF limit (10)
RP_CPX	IT $\&\&$!BBC-E $\&\&$!BBCW $\&\&$!ZDCE $\&\&$!ZDCW $\&\&$ TOF ≥ 2	40.1	The same as RP_CPT2 but only IT configuration
RP_CPEI	ET $\&\&$ IT $\&\&$!BBC-E $\&\&$!BBCW $\&\&$!ZDCE $\&\&$!ZDCW $\&\&$ TOF ≥ 2	15.6	Control trigger for CPT2 to estimate effect of !(ET $\&\&$ IT) veto

Table 2.1: Central Diffraction physics triggers and control triggers involving Roman Pot detectors in run 15.

2.2 Reconstruction software

Raw data was processed with STAR libraries in versions SL17f. All four trigger datasets were processed: production_pp200trans_2015, production_pp200long2_2015, production_pp200long3_2015 and production_pp200long_2015 (see [16]).

The following BFC options were used in the reconstruction:

```
DbV20160418,pp2015c,btof,mtd,mtdCalib,pp2pp,-beamline,beamline3D,useBTOFmatchOnly,VFStoreX,  
fmsDat,fmsPoint,fpsDat,BEmcChkStat,-evout,CorrX,OSpaceZ2,OGridLeak3D,-hitfilt
```

Main attention should be put on option **useBTOFmatchOnly** which forced vertexing algorithm to form vertices only from the global TPC tracks which are matched with hits in the TOF system. This solution was found to yield significantly larger signal reconstruction efficiency (vertexing efficiency) and better resolutions. The study which lead to above conclusions, presented in Ref. [17], was performed on the same dataset processed with older libraries SL15k (without useBTOFmatchOnly option).

2.3 Data format

The analyzed data was stored in ROOT files in the picoDST format which was in large part a skimmed MuDST (standard STAR format). The picoDST format was introduced in Ref. [18]. PicoDST description files (C++ headers etc.) can be found in the analysis code repository [19].

3. Event selection

Complete list of analysis cuts used for signal extraction is presented in Sec. 3.1. Detailed description of each cut can be found in Sec. 3.2.

3.1 List of cuts¹

C1. Exactly 1 primary vertex with TPC track(s) matched with hits in TOF.

C2. TPC vertex from C1 is placed within $|z_{\text{vx}}| < 80$ cm.

C3. Exactly 2 opposite-sign primary TPC tracks (C3.2) of good quality (C3.4) matched with hits in TOF (C3.1), reconstructed within kinematic region of high TPC acceptance (C3.3) and with small distance of closest approach (DCA) to the vertex (C3.5).

C3.1. Exactly 2 TOF-matched (match flag > 0) primary tracks and no additional primary tracks matched with BEMC clusters,

C3.2. Tracks are of opposite signs,

C3.3. Both tracks are contained within the kinematic range: $|\eta| < 0.7$, $p_T > 0.2$ GeV/ c ,

C3.4. Both tracks satisfy quality criteria: $N_{\text{hits}}^{\text{fit}} \geq 25$, $N_{\text{hits}}^{\text{dE/dx}} \geq 15$, $|d_0| < 1.5$ cm,

C3.5. Both tracks match well to the primary vertex: $\text{DCA}(R) < 1.5$ cm, $\text{DCA}(z) < 1$ cm.

C4. Exactly 1 RP track on each side of STAR central detector (C4.3) of good quality (C4.1), with local angles consistent with the IP being the track origin (C4.2), lying within fiducial region of high geometrical acceptance (C4.4).

C4.1. RP tracks contain only track-points with at least 3 (out of 4) planes used in reconstruction,

C4.2. Local angles (θ_x^{RP} , θ_y^{RP}) consistent with expectation for protons originating from the IP

$$-2 \text{ mrad} < \theta_x^{\text{RP}} - x^{\text{RP}}/|z^{\text{RP}}| < 4 \text{ mrad}, \quad -2 \text{ mrad} < \theta_y^{\text{RP}} - y^{\text{RP}}/|z^{\text{RP}}| < 2 \text{ mrad},$$

C4.3. Exactly 1 track passing cuts C4.1-C4.2 per side,

C4.4. Tracks passing cut C4.3 lie within the fiducial (p_x, p_y) region defined as:

$$0.2 < |p_y| < 0.4, \quad -0.2 < p_x, \quad (p_x + 0.3)^2 + p_y^2 < 0.5^2 \quad (\text{all in GeV}).$$

C5. Vertex z -positions measured in TPC and reconstructed from the difference of proton detection time in west and east RPs are consistent with each other within the resolution: $|z_{\text{vx}}^{\text{TPC}} - z_{\text{vx}}^{\text{RP}}| < 36$ cm ($3\sigma_{\Delta z_{\text{vtx}}}$).

C6. No signal in any tile of BBC-large (east or west) with $\text{ADC} > \text{ADC}_{\text{thr}}$ and $100 < \text{TDC} < 2400$, where ADC_{thr} is specific for each channel.

C7. Maximally 3 reconstructed TOF clusters $N_{\text{clstrs}}^{\text{TOF}} \leq 3$.

C8. Missing (total) momentum of TPC tracks and RP tracks $p_T^{\text{miss}} < 75$ MeV/ c .

C9. Particle (pair) identification:

C9.1. Identification of particle pairs based on dE/dx and m_{TOF}^2 :

```

if nσpionpair > 3 and nσkaonpair > 3 and nσprotonpair < 3 and mTOF2 > 0.6 GeV/c2 → p̄p
elif nσpionpair > 3 and nσkaonpair < 3 and nσprotonpair > 3 and mTOF2 > 0.15 GeV/c2 → K+K-
elif |nσpiontrk1| < 3 and |nσpiontrk2| < 3 → π+π-
else event rejected.

```

C9.2. Restricting fiducial cuts on K^+K^- and $p\bar{p}$:

```

if p̄p: pT > 0.4 GeV/c, min(pT+, pT-) < 1.1 GeV/c
if K+K-: pT > 0.3 GeV/c, min(pT+, pT-) < 0.7 GeV/c

```

¹Some cuts (e.g. C3) are decomposed to constituent sub-cuts. Cut is formed by the logical AND of all its sub-cuts. Events must pass all cuts to be identified as a signal.

3.2 Description of cuts

3.2.1 (C1,C2) Primary vertex and its z -position

As it was designed in the trigger logic, we aim to perform CEP analysis in a clean, pile-up-free environment, therefore we cut on primary vertex multiplicity (Fig. 3.1) to reject events with more than one interaction per bunch crossing. We require exactly one primary vertex containing TPC tracks matched with hits in TOF (matching of the track with hit in TOF is identified with the TOF match flag being different from 0). Later in the text we refer to such events as a single “TOF vertex” events.

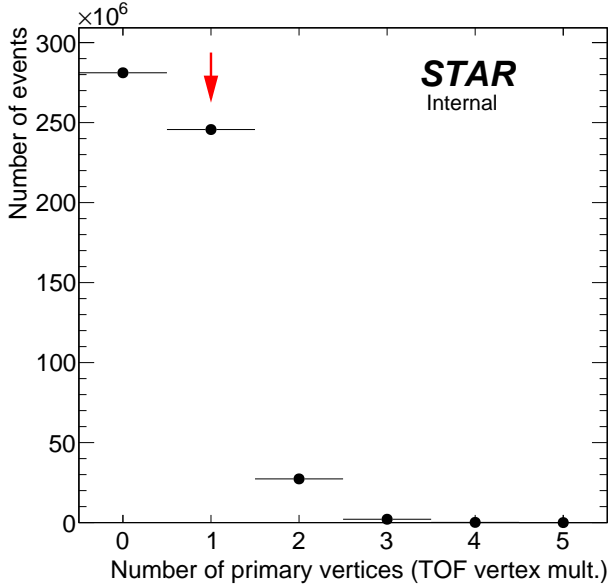


Figure 3.1: Primary vertex multiplicity. Red arrow marks bin with events with exactly one primary vertex (with track(s) matched with hit in TOF), which are used in physics analysis.

The single TOF vertex is required to be placed within a range (-80 cm, 80 cm) along the z -axis (Fig. 3.2). Events with vertices away from the nominal IP have low acceptance both for the central tracks and the forward protons (comparing to events with vertices close to nominal IP), therefore we reject them as their inclusion to analysis would naturally introduce large systematic uncertainties. See Sec. 3.2.3 in Ref. [1]

3.2.2 (C3) TPC tracks

The TPC track selection starts from the selection of events with exactly two primary tracks matched with hit in TOF (Fig. 3.3). Matching with TOF guarantee that analyzed tracks originate from the triggered bunch crossing (ensures that tracks are “in-time”). It is in accordance with the trigger logic which required at least 2 L0 TOF hits, as well as it enables more accurate particle identification with merged time-of-flight and dE/dx method, comparing to sole usage of dE/dx . Primary tracks not matched with hit in TOF, whose average multiplicity in single TOF vertex is ~ 8 , are hardly distinguished between real and fake (off-time) tracks, which is an additional reason for not analyzing events with only one TOF-matched primary TPC track (the other track might be unmatched due to TOF inefficiency).

Primary TPC tracks from the single TOF vertex which are matched with TOF are allowed to be also matched with BEMC clusters. Matching with BEMC cluster is claimed if the distance in $\eta - \phi$ space between the BEMC cluster position (η_{clus} , ϕ_{clus}) and projected position of the track in BEMC (η_{proj} , ϕ_{proj}), defined as

$$R = \sqrt{(\eta_{\text{clus}} - \eta_{\text{proj}})^2 + (\phi_{\text{clus}} - \phi_{\text{proj}})^2}, \quad (3.1)$$

is less than $R_{\text{max}}^{\text{match}} = 0.05$. Distribution of the distance between the primary TPC track and the closest BEMC cluster is shown in Fig. 3.4.

However, if there are any primary TPC tracks matched with BEMC cluster and not matched with TOF in the single TOF vertex with two TOF-matched tracks, an event is rejected. Such configuration implies higher-than-2 multiplicity of the real tracks in the vertex, hence an event is unlikely a Central Exclusive Production of two particles.



Figure 3.3: Multiplicity of primary TPC tracks matched with hit in TOF for single TOF vertex events. Red arrow marks bin with events with exactly two primary tracks matched with hit in TOF, which are used in physics analysis.



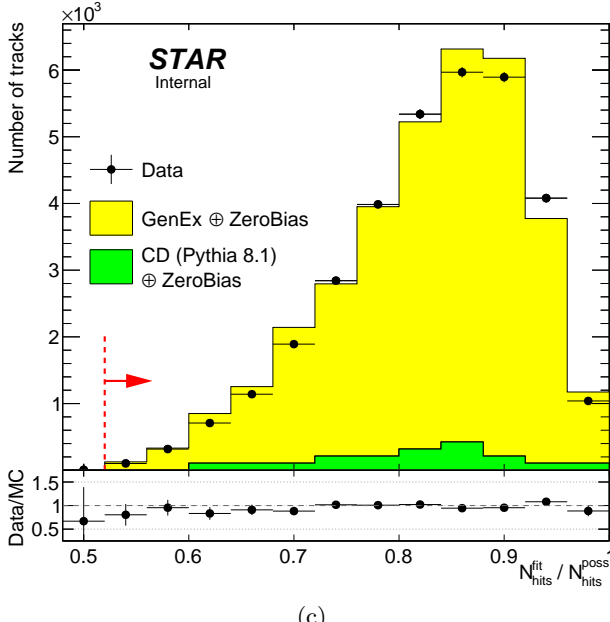
Figure 3.4: Distribution of a distance in $\eta - \phi$ space between the BEMC cluster closest to primary TPC track matched (filled circle) or not matched (open circle) with hit in TOF, for single TOF vertex events. Red dashed line indicate matching threshold $R_{\max}^{\text{match}} = 0.05$.



(a)



(b)



(c)

Figure 3.5: Comparison of distribution of the number of hits used in TPC track reconstruction $N_{\text{hits}}^{\text{fit}}$ (3.5a), number of hits used in specific energy loss reconstruction $N_{\text{hits}}^{\text{dE/dx}}$ (3.5b) and fraction of number of hits potentially generated by the track and finally used in the reconstruction $N_{\text{hits}}^{\text{fit}} / N_{\text{hits}}^{\text{poss}}$ (3.5c) in the data and embedded MC. Normalizations of the signal and backgrounds were established from the comparison of p_T^{miss} and $\Delta\theta$ distributions after full selection (without cut on the presented quantity and without exclusivity cut), as described in Sec. 5.2. Red dashed line and red arrow indicate the range of each quantity which is accepted in analysis.



Figure 3.6: Comparison of the track pseudorapidity η (3.6a) and the track azimuthal angle ϕ (3.6b) in the data and embedded MC. Normalizations of the signal and backgrounds were established from the comparison of p_T^{miss} and $\Delta\theta$ distributions after full selection (without cut on the presented quantity and without exclusivity cut), as described in Sec. 5.2. Red dashed lines and red arrows indicate the range of each quantity which is accepted in analysis.

3.2.3 (C4) RP tracks

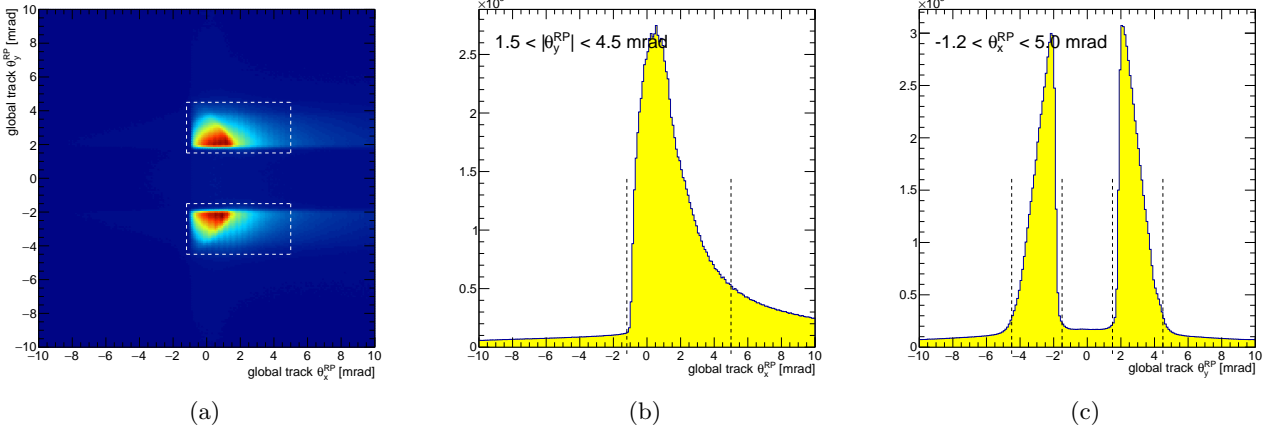


Figure 3.7: Local angles of global tracks in Roman Pots.

3.2.4 (C5) TPC-RP z -vertex matching

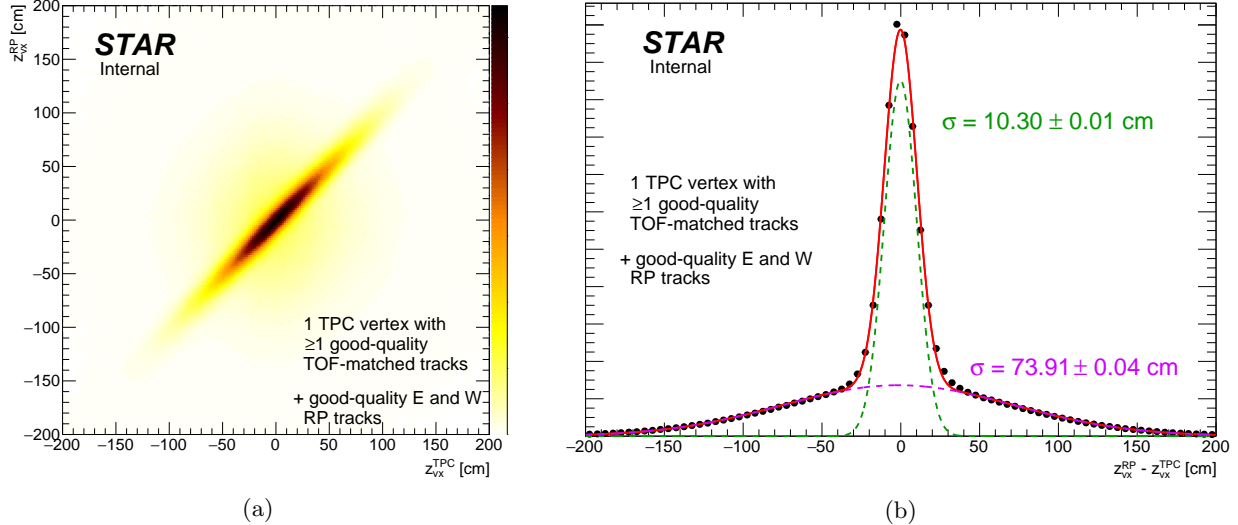


Figure 3.8: Correlation (Fig. 3.8a) and difference (Fig. 3.8b) of z -vertex position measured in Roman Pots and TPC.

3.2.5 (C6) BBC-large signal veto

At the trigger level a veto on signal in small BBC detectors was used. During offline analysis we found that the non-exclusive background can be efficiently rejected if an additional veto on signal in large BBC detectors is added. It is connected with the fact that vast majority of selected RP_CPT2 triggers were from the central diffraction process to which CEP belongs. Many of central diffraction events have particles produced in the rapidity region outside the TPC and TOF acceptance, some hitting large BBC tiles. Presence of signal in large BBC is therefore a signature of background or a pile-up interaction.

The response of large BBC tiles is different from that of small BBC tiles, as shown in sample plots in Fig. ?? (similar distributions for all channels can be found in Appendix A). Typically in small BBC tiles a peak visible in ADC distribution around 100 – 150 (Figs. 3.9a,3.9c), a signature of good separation of the electronics noise and signal from the ionizing particle. No such feature is observed in corresponding distribution for large BBC tile (Figs. 3.9b,3.9d), which can be explained by the difference in geometry (in size) of small and large tiles. In large BBC tiles the path that scintillation light must travel to reach PMT is much longer in comparison to small BBC tiles (multiple reflections on the main tile surface due to small thickness of the tile) therefore it is highly

attenuated and extended in time. This is possible reason of lack of signal peak in the ADC distribution in large BBC tile spectrum (Fig. 3.9d), as well as the late-TAC (TAC < ~600, ADC < 100) tail in the ADC vs. TAC spectrum (slewing effect, Fig. 3.9b). Nevertheless, the above features of BBC-large response does not disqualify this detector from being used as a veto detector, as in this case lower efficiency of the detector only reduce the background rejection power.

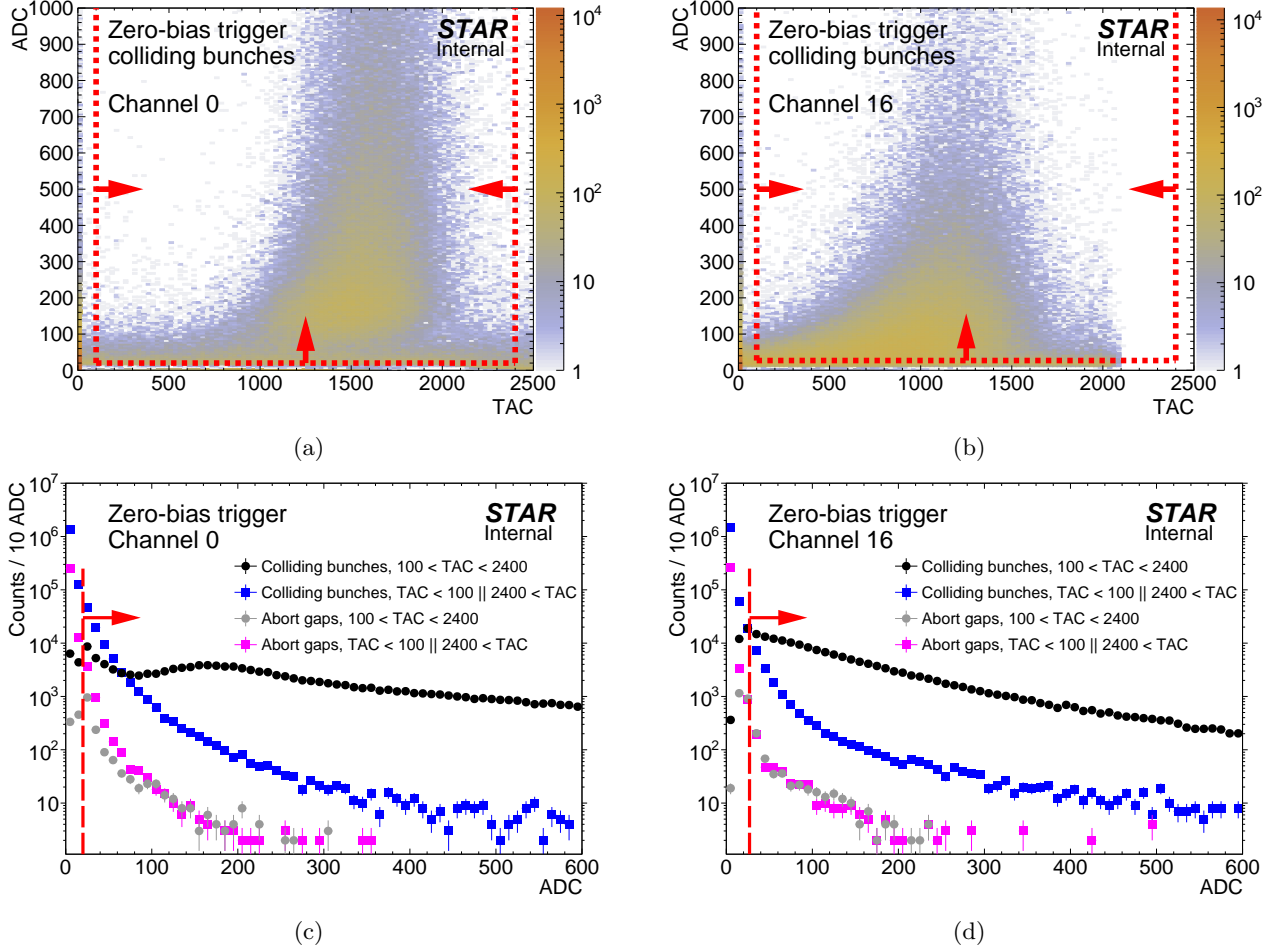


Figure 3.9: Sample BBC-small (left column) and BBC-large (right column) response in zero-bias data. Top row shows TAC vs. ADC distributions, bottom row shows projection of the corresponding two-dimensional distribution on x -axis (ADC) in the TAC range quoted in the legend, for both abort gaps and colliding bunches. Red lines and arrows indicate thresholds for a signal in presented channels.

Each channel of the BBC-large has different response to signal from ionizing particle, as well as different level of noise. We decided to set up a signal threshold for each channel based on a study of the noise in abort gaps (in zero-bias data). This noise, in principle, should be solely the electronics noise. We checked for each channel the probability to detect a signal with ADC above certain threshold and with TAC contained within 100 and 2400 (the same window is default for small BBC). The result is shown in Fig. 3.10. Next, we established final ADC thresholds in each BBC-large channel by requiring that the noise in BBC-large would cause a veto in maximally 3.5% of events. To transform it to ADC_{thr} we first assumed that the noise is uncorrelated between the channels. With this assumption one can connect the probability of the veto in whole BBC-large detector (east and west) caused by noise $\mathcal{P}_{\text{veto}}^{\text{noise}}$ with the probability of the signal induced by noise in single BBC-large channel $\mathcal{P}_{i,\text{sig}}^{\text{noise}}$:

$$\mathcal{P}_{\text{veto}}^{\text{noise}} = 1 - \mathcal{P}_{\text{veto}}^{\text{noise}} = 1 - (1 - \mathcal{P}_{i,\text{sig}}^{\text{noise}})^{N_{\text{ch}}^{\text{BBC}}}. \quad (3.2)$$

In the equation above $N_{\text{ch}}^{\text{BBC}}$ denotes number of active channels in BBC-large. From plots contained in Appendix A one can read that there were 14 active channels in BBC-large. 2 dead channels were found on the west side (40 and 42). By transforming Eq. 3.2 to the form presented below we can calculate the threshold probability for a single BBC-large channel:

$$\mathcal{P}_{i,\text{sig}}^{\text{noise}} = 1 - \sqrt[N_{\text{ch}}^{\text{BBC}}]{1 - \mathcal{P}_{\text{veto}}^{\text{noise}}} = 1 - \sqrt[14]{1 - 0.035} \approx 0.0025. \quad (3.3)$$

In the last step we translated this number to ADC threshold for each channel of BBC-large. For this purpose we used Fig. 3.10. The x -axis projection of the crossing point of each color line with the y -axis value of 0.0025 defines ADC_{thr} for each particular channel. These numbers are listed in Tab. 3.1. The event was dropped from analysis if any of the BBC-large channels registered signal of strength $\text{ADC}_i > \text{ADC}_{i,\text{thr}}$ and $100 < \text{TAC}_i < 2400$.

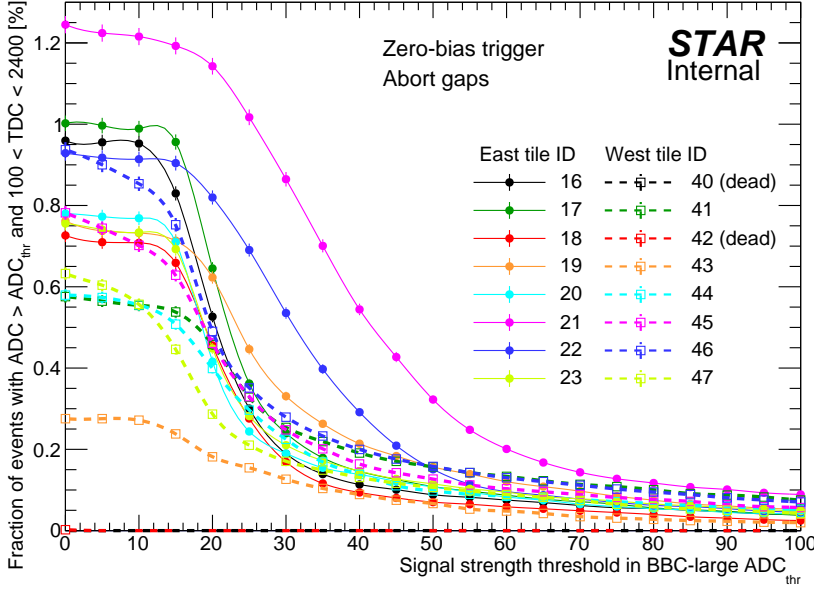


Figure 3.10: Percentage of events in abort gaps from zero-bias triggers with the ADC counts larger than the ADC threshold given in the x -axis, for each BBC-large channel. Measured points with statistical uncertainties are connected with a smooth line of corresponding color for better visualization.

Observation of high purification of CEP sample with described BBC-large veto in the data from run 15 was helpful to improve the CEP trigger for run 17. The improved trigger called RP_CPT2noBBCL was similar to RP_CPT2 with an addition of BBC-large veto using ADC threshold of 50.

3.2.6 (C7) TOF clusters limit

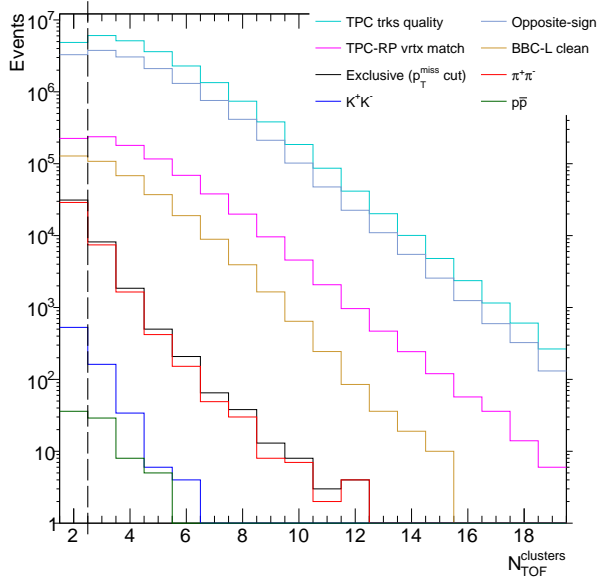


Figure 3.11: NTofClusters.

East		West	
i	ADC_{thr}	i	ADC_{thr}
16	27	40	0
17	30	41	31
18	26	42	0
19	37	43	14
20	25	44	29
21	55	45	30
22	43	46	33
23	27	47	22

Table 3.1: Offline ADC thresholds in BBC-large.

3.2.7 (C8) Exclusivity cut (missing p_T cut)

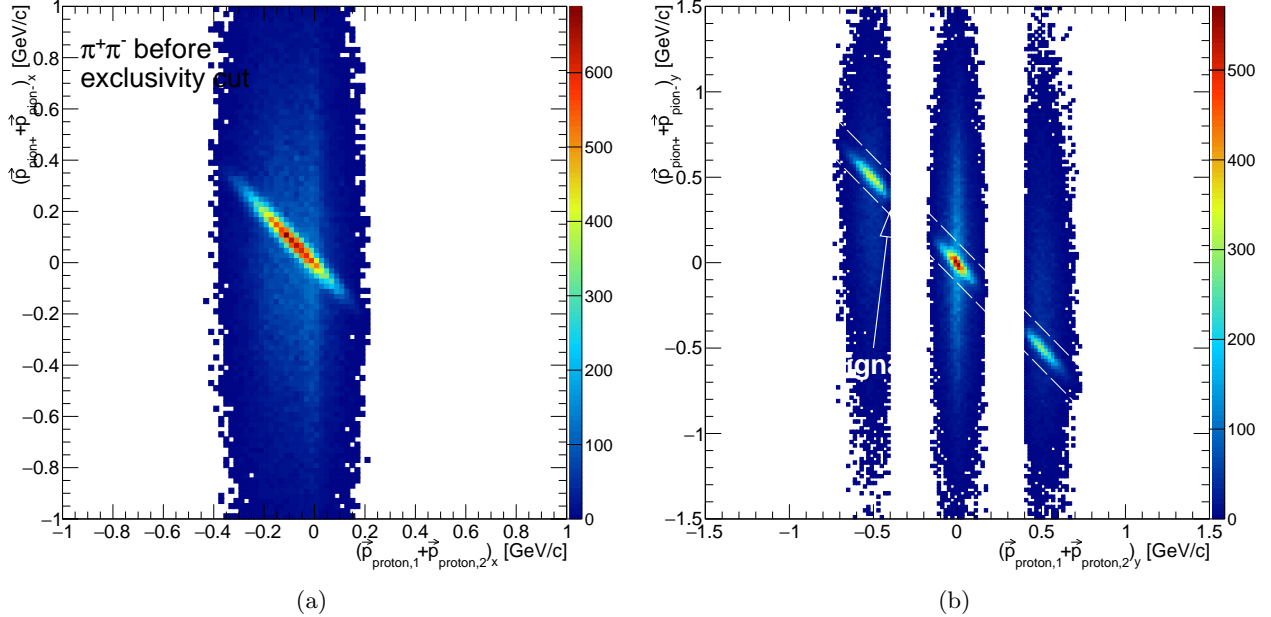


Figure 3.12: Correlation between sum of corresponding momentum components (x in Fig. 3.12a and y in Fig. 3.12b) of Roman Pot proton tracks and TPC tracks.

Tutaj dodac rysunki z suma 1D tych wielkosci i uzasadnic stosowanie ciecia na missing pT takimi samymi rozdzielczosciami w x i y

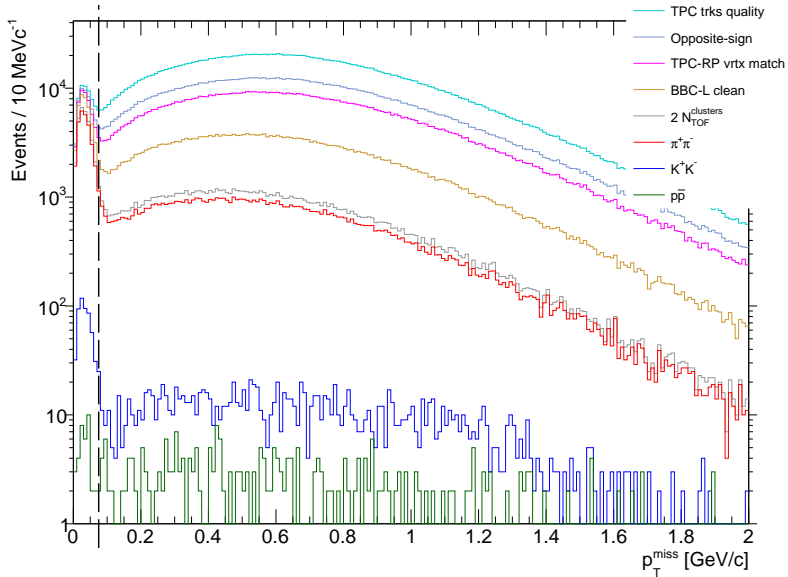


Figure 3.13: MissingPt.

3.2.8 (C9) Particle identification

In addition to information from the TPC we use time of hit detection in the barrel TOF subsystem.

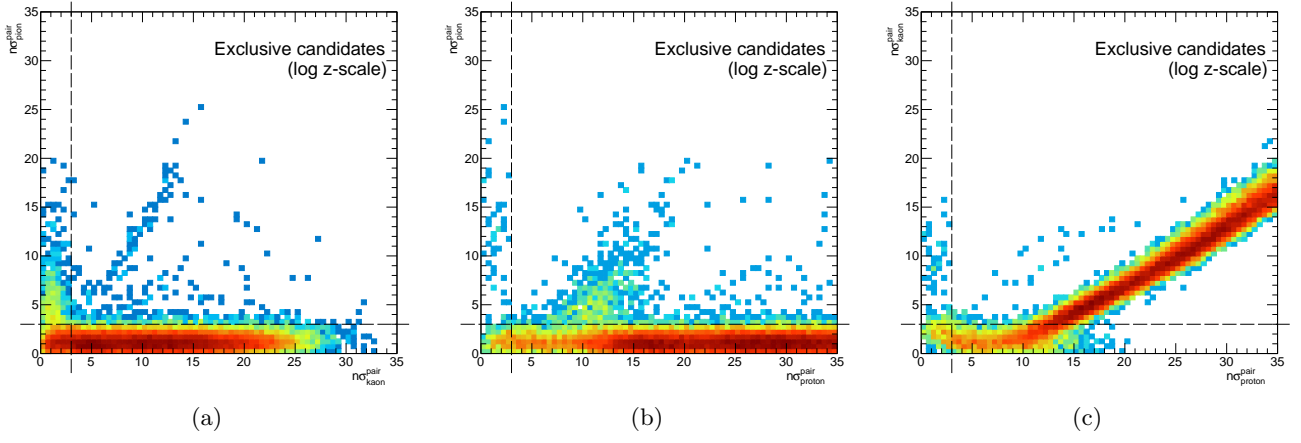


Figure 3.14: Correlation between $n\sigma^{\text{pair}}$ from TPC for $\pi^+\pi^-$, K^+K^- and $p\bar{p}$.

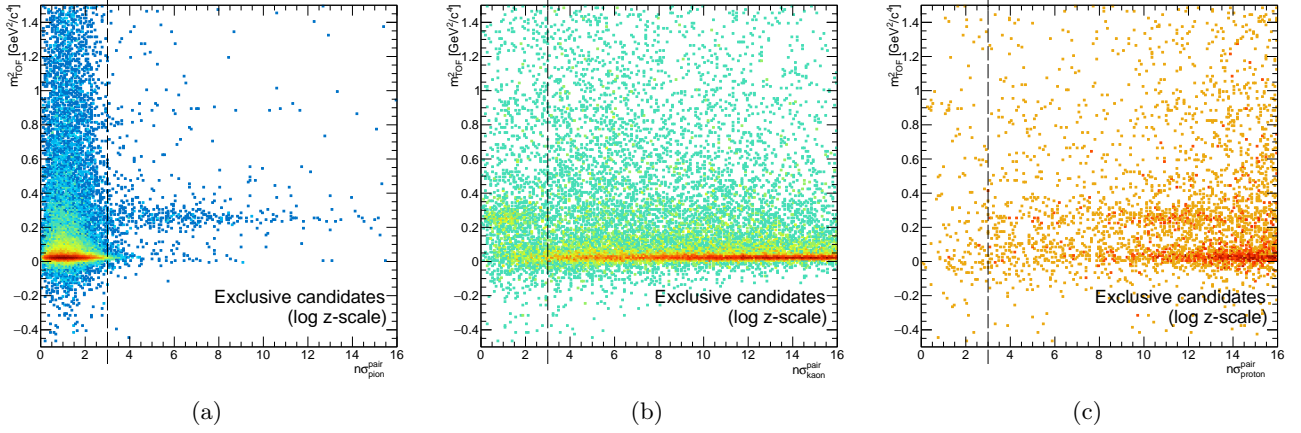


Figure 3.15: Correlation between m^2 from TOF and $n\sigma^{\text{pair}}$ from TPC for $\pi^+\pi^-$, K^+K^- and $p\bar{p}$.

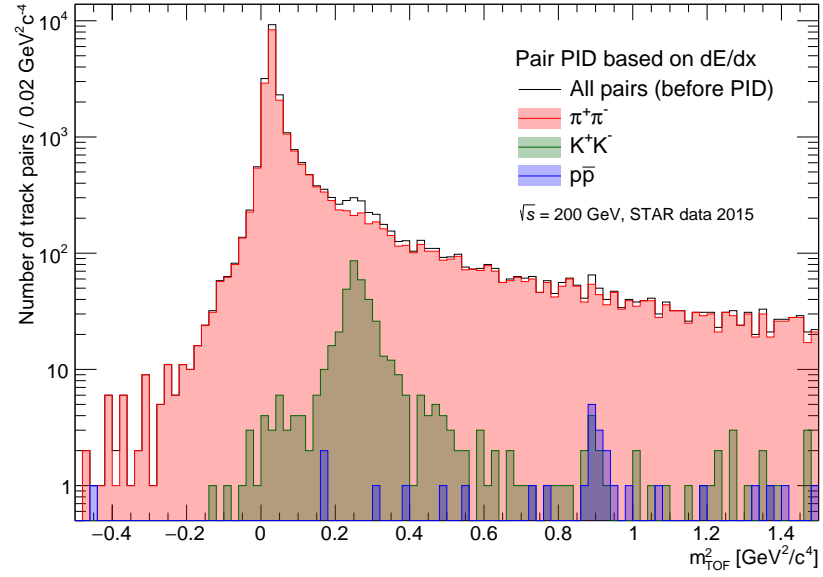
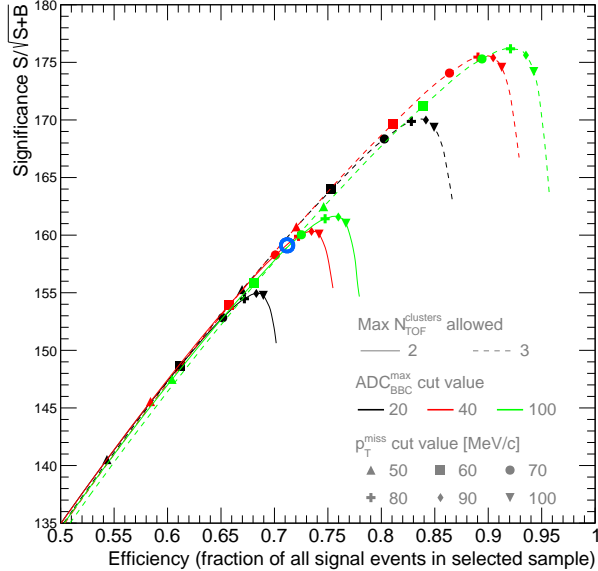


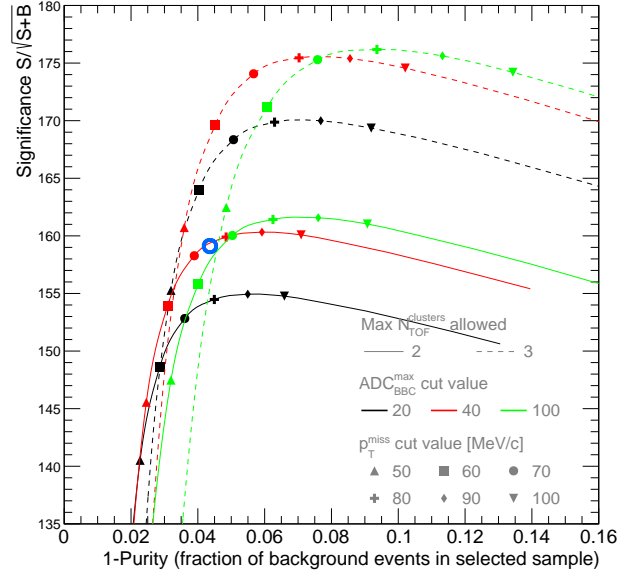
Figure 3.16: Squared particle mass from TOF for candidates of given PID selected based on dE/dx in TPC.

3.3 Working point for cuts C6, C7 and C8

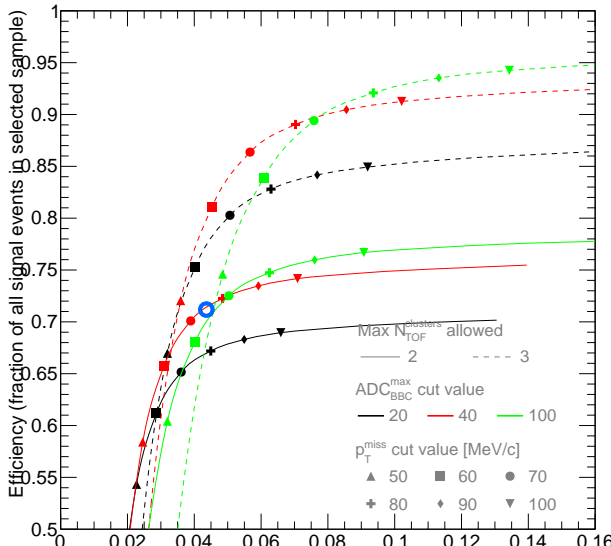
$$\text{Significance} = \frac{N_{\text{signal}}^{\text{cut}}}{\sqrt{N_{\text{signal}}^{\text{cut}} + N_{\text{bkgd}}^{\text{cut}}}}, \quad (3.4) \quad \text{Efficiency} = \frac{N_{\text{signal}}^{\text{cut}}}{N_{\text{signal}}^{\text{no cut}}}, \quad (3.5) \quad \text{Purity} = \frac{N_{\text{signal}}^{\text{cut}}}{N_{\text{signal}}^{\text{cut}} + N_{\text{bkgd}}^{\text{cut}}}, \quad (3.6)$$



(a)



(b)



(c)

Figure 3.17: Relation between $\pi^+\pi^-$ signal significance and efficiency (3.17a), significance and purity (3.17b), and efficiency and purity (3.17c) as a function of cut thresholds in BBC-large veto (C6), TOF cluster limit (C7) and exclusivity cut (C8). Lines show forementioned relations with changing p_T^{miss} cut whose some specific values are indicated with different markers. Color denotes ADC threshold in BBC-large veto (black, red or green). Style of line (solid or dashed) denotes $N_{\text{clstrs}}^{\text{TOF}}$ limit. Working point considered optimal is marked with opened blue circle.

3.4 Signal per integrated luminosity

3.5 Cut flow

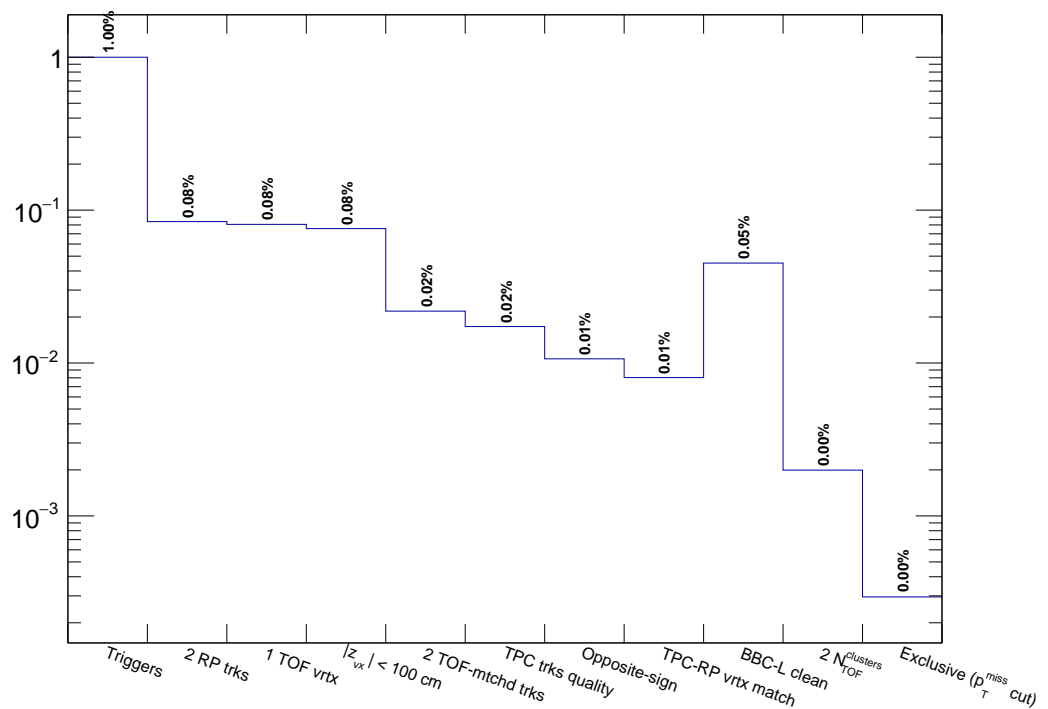


Figure 3.18: Cut flow.

4. Corrections

4.1 Method of corrections application

$$\frac{d\sigma}{dq} = \frac{1}{\Delta q} \times \frac{1}{\varepsilon} \times \frac{N^w - N_{\text{bkgd}}^w}{L_{\text{int}}^{\text{eff}}} \quad (4.1)$$

$$L_{\text{int}}^{\text{eff}} = \sum_{\text{run}} L_{\text{int}}^{\text{run}} \times \epsilon_{\text{veto}}(L^{\text{run}}) \quad (4.2)$$

$$\varepsilon = \epsilon_{\text{ET/IT}} \times \epsilon_{\text{vrtx}}(q) \times \epsilon_{C2} \times \epsilon_{C5} \times \epsilon_{C8} \times \epsilon_{\text{PID}}(q) \quad (4.3)$$

$$N^w = \sum_{\text{event}} w_{\text{event}} \quad (4.4)$$

$$w = \left[\prod_{\text{sign}} \epsilon_{\text{TOF}}(\text{sign}, \text{PID}, p_T, z_{vx}, \eta) \times \prod_{\text{sign}} \epsilon_{\text{TPC}}(\text{sign}, \text{PID}, p_T, z_{vx}, \eta) \times \prod_{\text{side}} \epsilon_{\text{RP}}^{\text{side}}(p_x, p_y) \right]^{-1}, \quad (4.5)$$

$\text{sign} \in \{+, -\}, \quad \text{side} \in \{E, W\}$

4.2 Efficiencies and acceptances

In this section we present calculation of all efficiencies except TPC track reconstruction and TOF hit reconstruction and matching efficiency, which were discussed and presented in Ref. [1].

4.2.1 Trigger efficiency

4.2.1.1 Online veto (BBC-small and ZDC veto)

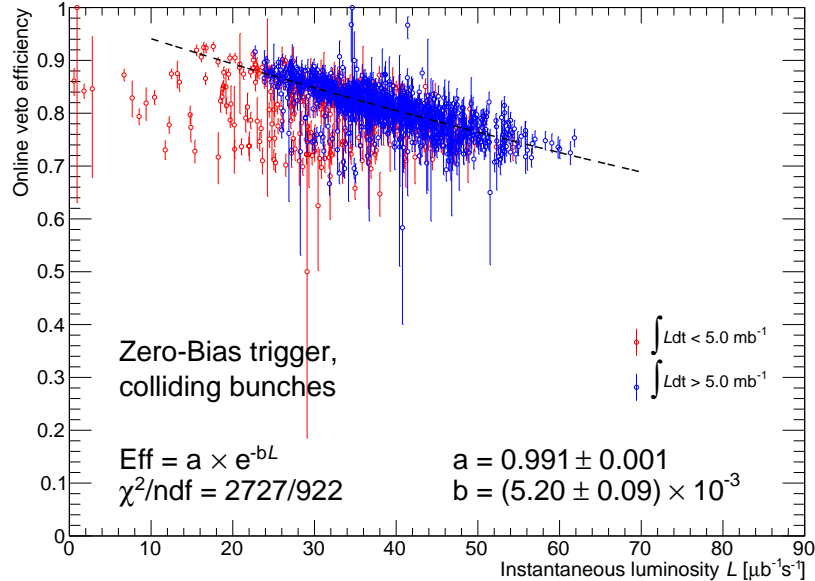
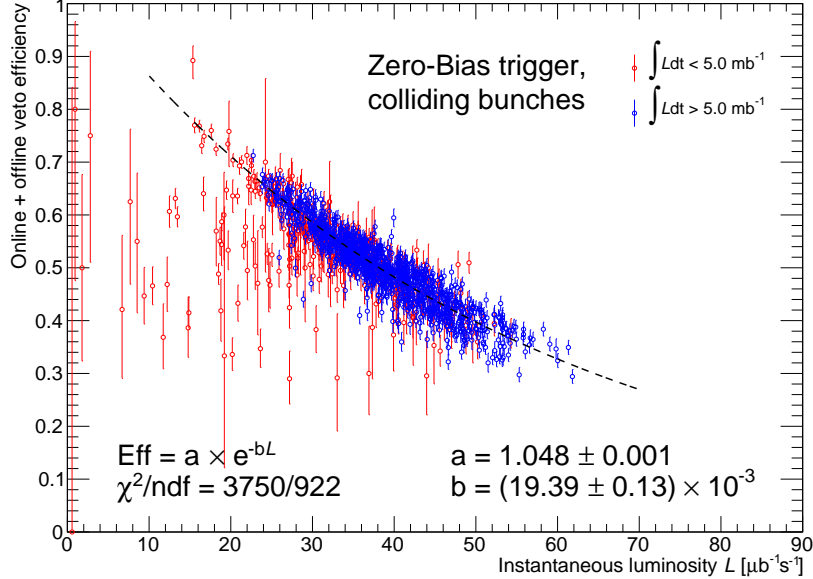


Figure 4.1: Overall efficiency of the online BBC-small and ZDC veto as a function of instantaneous luminosity.

- 4.2.1.2 RP triggering efficiency
- 4.2.1.3 Up and Down RP combination veto
- 4.2.2 Cuts efficiency
 - 4.2.2.1 TPC z -vertex cut (C2)
 - 4.2.2.2 TPC-RP z -vertex matching (C5)
 - 4.2.2.3 Primary vertices limit (C1), BBC-large veto (C6) and TOF clusters limit (C7)



- 4.2.2.4 Missing p_T cut (C8)
- 4.2.2.5 Particle identification (C9)

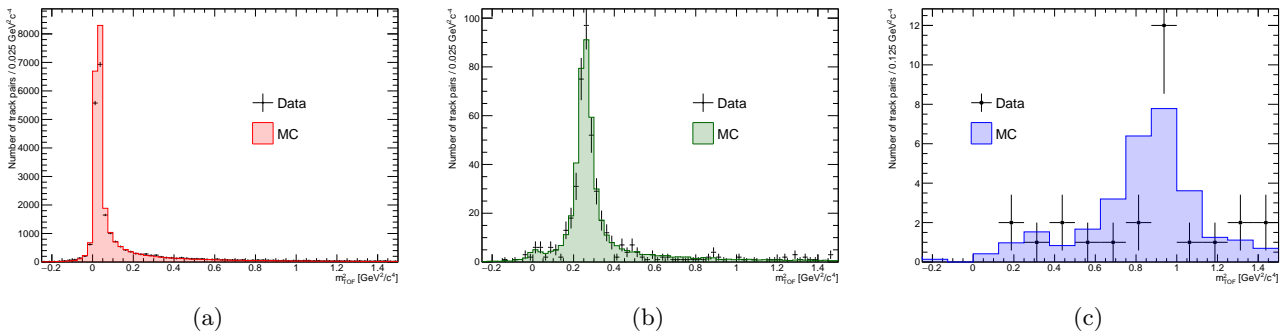


Figure 4.3: Comparison of m^2 from TOF between data and MC for exclusive $\pi^+\pi^-$, K^+K^- and $p\bar{p}$.

4.2.3 RP track acceptance and reconstruction efficiency

To calculate RP acceptance and track reconstruction efficiency the embedded MC technique was used (see Sec. 6.3 in Ref. [1] for details of RP simulation in Geant4). Forward protons from CEP process provided by GenEx [20] were simultaneously generated from the interaction point spatially distributed the same as in the data. MC samples for all runs with RP_CPT2 triggers were produced to account for non-constant positions of the RP detectors throughout the run 15. Number of simulated events for each run was proportional to number of RP_CPT2 triggers in given run. The angular divergence of the beams was also simulated.

The joint RP acceptance and track reconstruction efficiency for a given STAR side, $\epsilon_{\text{RP}}^{\text{side}}$, was calculated as a probability that a single good quality RP track (satisfying cuts C4.1-C4.2) matched with true-level primary forward proton is reconstructed on given side in the branch expected based on sign of p_y of the proton, under condition that there is a trigger signal in that branch and there is no trigger signal in the other branch on the same side.

Technically the $\epsilon_{\text{RP}}^{\text{side}}$ was obtained in the following procedure:

1. It was verified if there is a trigger signal in the branch that the primary forward proton is expected to reach based on its p_y ($p_y > 0$ - branch UP, $p_y < 0$ - branch DOWN). Additionally required lack of trigger signal in the other branch on the same side. These events formed *set A*.
2. The nominal RP track selection algorithm was used to find a single good quality track (cuts C4.1-C4.2) on given side. If exactly one such track was found, it was additionally checked if it is matched with true-level primary proton. These events formed *set B*.
3. The efficiency was calculated by the ratio of histograms from *set B* and *set A*:

$$\epsilon_{\text{RP}}^{\text{side}}(p_x, p_y, z_{\text{vtx}}) = \mathcal{E} \left(\text{RP}^{\text{side}} \mid \text{TR}^{\text{side}} \wedge \neg \text{TR}^{\text{side}} \right) = \frac{(p_x, p_y, z_{\text{vtx}}) \text{ histogram for protons from set } B}{(p_x, p_y, z_{\text{vtx}}) \text{ histogram for protons from set } A} \quad (4.6)$$

It should be noted that the momentum components (p_x, p_y) were taken from the proton with accounted effect of the beam divergence (after the original initial momentum smearing).

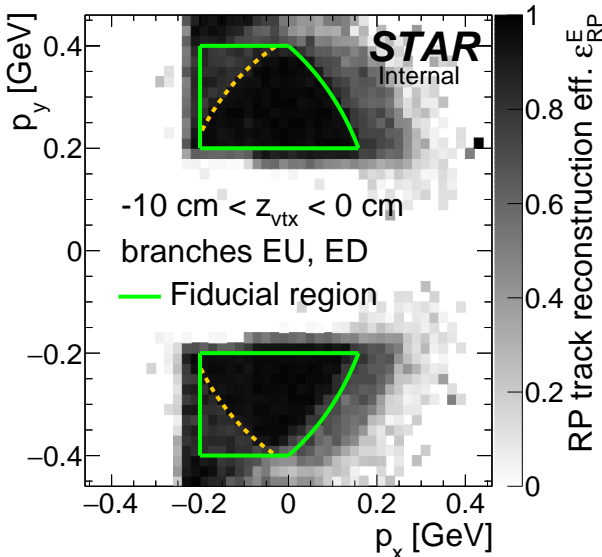


Figure 4.4: Sample RP track reconstruction efficiency in a single z -vertex bin on the east STAR side. The efficiency was calculated using forward proton MC simulation embedded into zero-bias data. Green envelopes mark the fiducial region of the measurement, while dashed yellow lines mark the part of the fiducial region with a data-driven efficiency correction needed, as explained in Sec. 10.3.1 of Ref. [1].

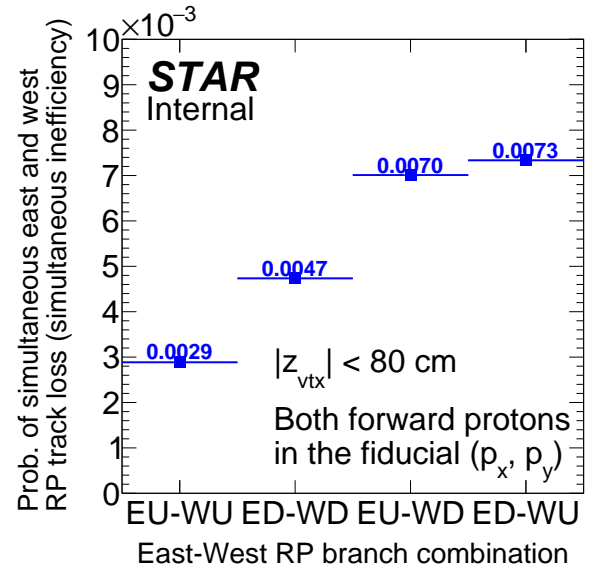


Figure 4.5: Probability of simultaneous inefficiency of the RP track reconstruction calculated from the CEP MC embedded into zero-bias data.

The efficiency calculated in the way described above is, by design, the acceptance, reconstruction and selection efficiency for a single proton on one side of the IP. In CEP event there are two independent forward protons which may be simultaneously not reconstructed or rejected by the selection algorithm due to e.g. elastic pile-up interaction providing additional good quality proton tracks on both sides of IP. One could, in principle, calculate 5-dimensional efficiency for both forward protons (in variables $p_x^{\text{E}}, p_y^{\text{E}}, p_x^{\text{W}}, p_y^{\text{W}}$ and z_{vtx}) which would ultimately account for the simultaneous east and west inefficiency, however this would require orders of magnitude larger statistics of MC to provide reasonably low statistical uncertainty of the efficiency. Instead, on top of the 3-dimensional reconstruction and selection efficiencies for east and west RPs we calculate (from embedded MC) probability that the proton tracks are simultaneously not reconstructed or selected on the east

and west side, despite the trigger signal solely in expected RP branches (no trigger veto) and true-level (p_x, p_y) of both forward protons contained in the fiducial region. This probability, denoted as

$$\mathcal{P}_{\text{loss}}^{\text{E\&W}} = \mathcal{E} \left(!\text{RP}^{\text{E}} \wedge !\text{RP}^{\text{W}} \mid \text{TR}^{\text{E}} \wedge \text{TR}^{\text{W}} \wedge !\text{Veto} \right), \quad (4.7)$$

is presented in Fig. 4.5 for all four combinations of east and west RP branches.

4.2.4 TPC vertex reconstruction efficiency

The definition of vertex reconstruction efficiency established in this analysis is the probability that two global tracks, both associated with true-level primary particles from the kinematic region of the measurement, both satisfying kinematic and quality criteria (cuts C3.3 and C3.4) and both matched with hits in TOF, form a vertex listed in the collection of reconstructed primary vertices and DCA(R) and DCA(z) of both global tracks calculated w.r.t. this vertex is contained within the limits of cut C3.5.

4.3 Particle energy loss

4.4 Background subtraction

5. Backgrounds

5.1 Sources of background

5.1.1 Non-exclusive background

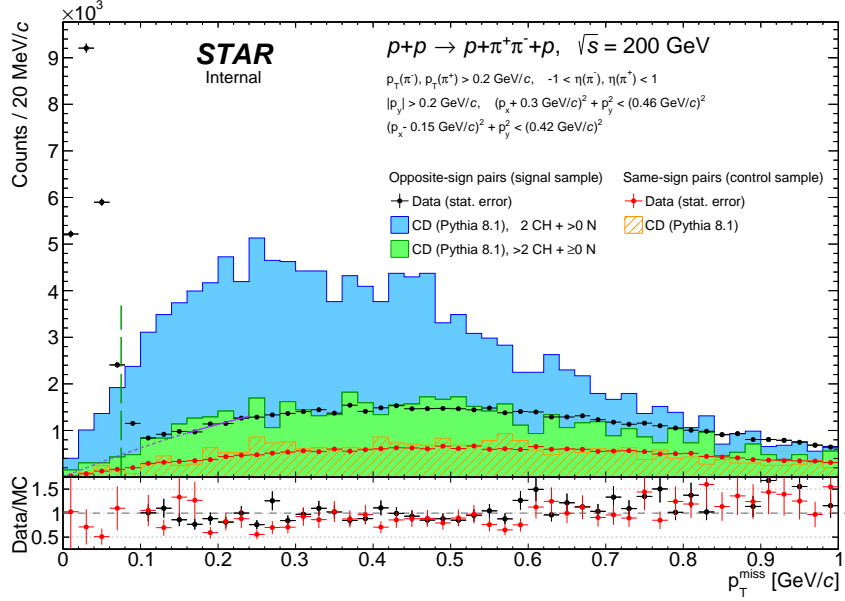


Figure 5.1: Missing pT.

tutaj dodac szkice spodziewanego tla nieekskluzywnego

5.1.2 Exclusive background (particle misidentification)

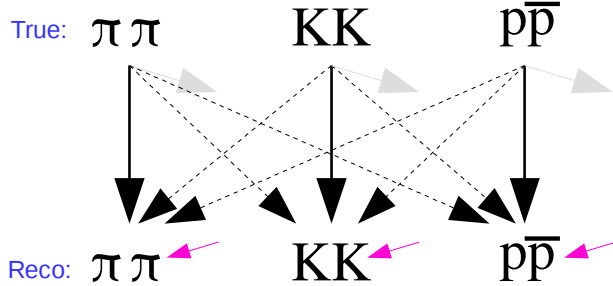


Figure 5.2: Graph illustrating the misidentification problem - the origin of exclusive background in selected samples. Gray arrows represent event rejection due to failed PID selection (C9). Magenta arrows indicate non-exclusive backgrounds described in Sec. 5.1.1. Solid black arrows represent successful identification, whereas dashed black lines show misidentification paths.

$$N_R^{\pi\pi} = \underbrace{\epsilon^{\pi\pi} \cdot N_T^{\pi\pi}}_{\text{true pion pairs}} + \underbrace{\lambda^{KK \rightarrow \pi\pi} \cdot N_T^{KK}}_{\text{kaon pairs reconstructed as pion pairs}} + \underbrace{\lambda^{p\bar{p} \rightarrow \pi\pi} \cdot N_T^{p\bar{p}}}_{\text{proton pairs reconstructed as pion pairs}} + N_{bkgd}^{\pi\pi} \quad (5.1a)$$

$$N_R^{KK} = \underbrace{\lambda^{\pi\pi \rightarrow KK} \cdot N_T^{\pi\pi}}_{\text{pion pairs reconstructed as kaon pairs}} + \underbrace{\epsilon^{KK} \cdot N_T^{KK}}_{\text{true kaon pairs}} + \underbrace{\lambda^{p\bar{p} \rightarrow KK} \cdot N_T^{p\bar{p}}}_{\text{proton pairs reconstructed as kaon pairs}} + N_{bkgd}^{KK} \quad (5.1b)$$

$$N_R^{p\bar{p}} = \underbrace{\lambda^{\pi\pi \rightarrow p\bar{p}} \cdot N_T^{\pi\pi}}_{\text{pion pairs reconstructed as proton pairs}} + \underbrace{\lambda^{KK \rightarrow p\bar{p}} \cdot N_T^{KK}}_{\text{kaon pairs reconstructed as proton pairs}} + \underbrace{\epsilon^{p\bar{p}} \cdot N_T^{p\bar{p}}}_{\text{true proton pairs}} + N_{bkgd}^{p\bar{p}} \quad (5.1c)$$

Eqs. (5.1) can be written in the matrix form, as shown in Eq. (5.2), from which it is straightforward to obtain final formula for unfolded number of events of given ID, Eq. (5.3):

$$\begin{bmatrix} N_R^{\pi\pi} - \textcolor{magenta}{N}_{bkgd}^{\pi\pi} \\ N_R^{KK} - \textcolor{magenta}{N}_{bkgd}^{KK} \\ N_R^{p\bar{p}} - \textcolor{magenta}{N}_{bkgd}^{p\bar{p}} \end{bmatrix} = \underbrace{\begin{bmatrix} \epsilon^{\pi\pi} & \lambda^{KK \rightarrow \pi\pi} & \lambda^{p\bar{p} \rightarrow \pi\pi} \\ \lambda^{\pi\pi \rightarrow KK} & \epsilon^{KK} & \lambda^{p\bar{p} \rightarrow KK} \\ \lambda^{\pi\pi \rightarrow p\bar{p}} & \lambda^{KK \rightarrow p\bar{p}} & \epsilon^{p\bar{p}} \end{bmatrix}}_{\text{"mixing matrix" } \Lambda} \begin{bmatrix} N_T^{\pi\pi} \\ N_T^{KK} \\ N_T^{p\bar{p}} \end{bmatrix} \rightarrow \begin{bmatrix} N_T^{\pi\pi} \\ N_T^{KK} \\ N_T^{p\bar{p}} \end{bmatrix} = \Lambda^{-1} \begin{bmatrix} N_R^{\pi\pi} - \textcolor{magenta}{N}_{bkgd}^{\pi\pi} \\ N_R^{KK} - \textcolor{magenta}{N}_{bkgd}^{KK} \\ N_R^{p\bar{p}} - \textcolor{magenta}{N}_{bkgd}^{p\bar{p}} \end{bmatrix} \quad (5.2)$$

5.2 Relative normalization of background and signal

6. Systematic errors

7. Physics results

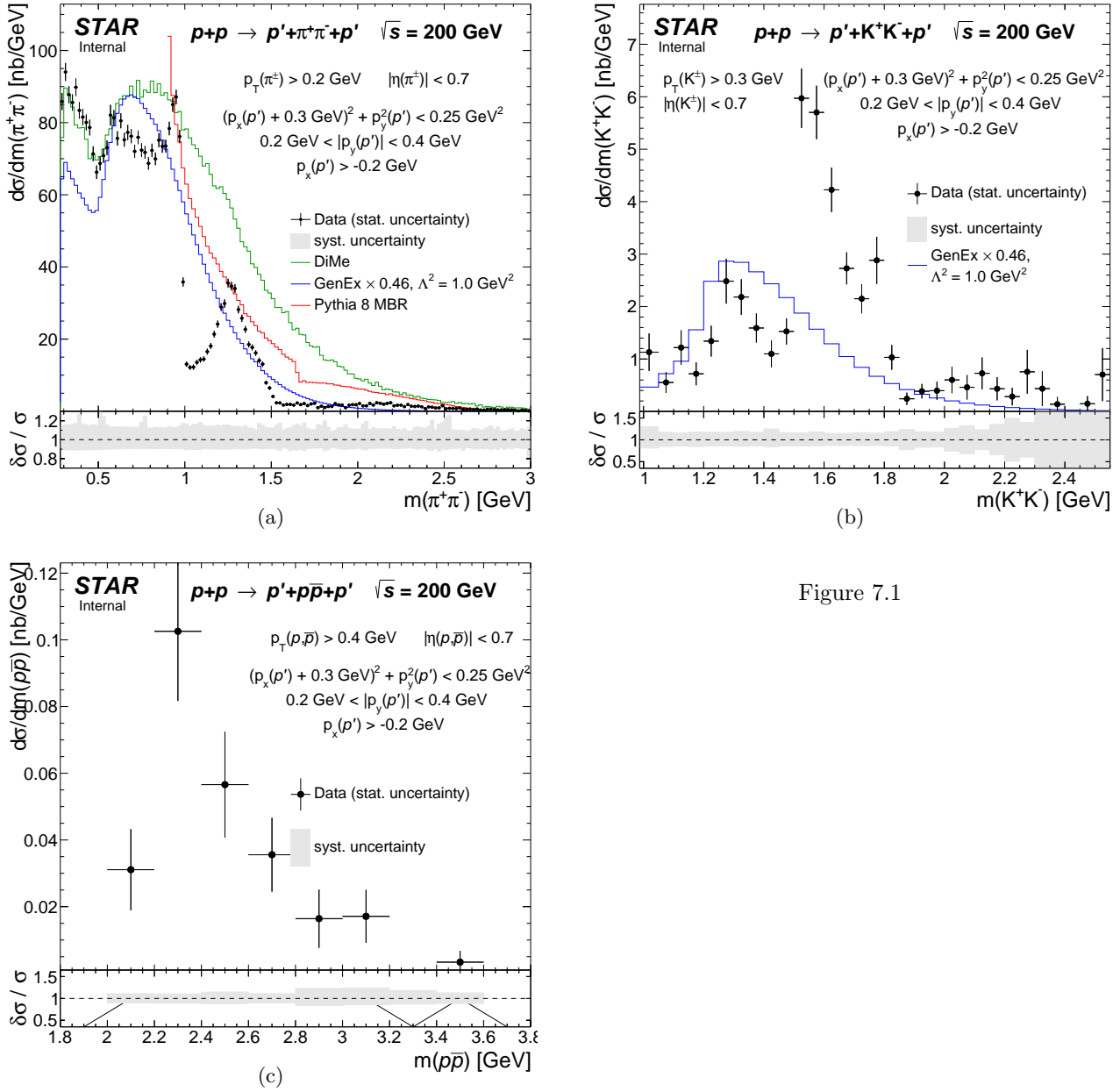


Figure 7.1

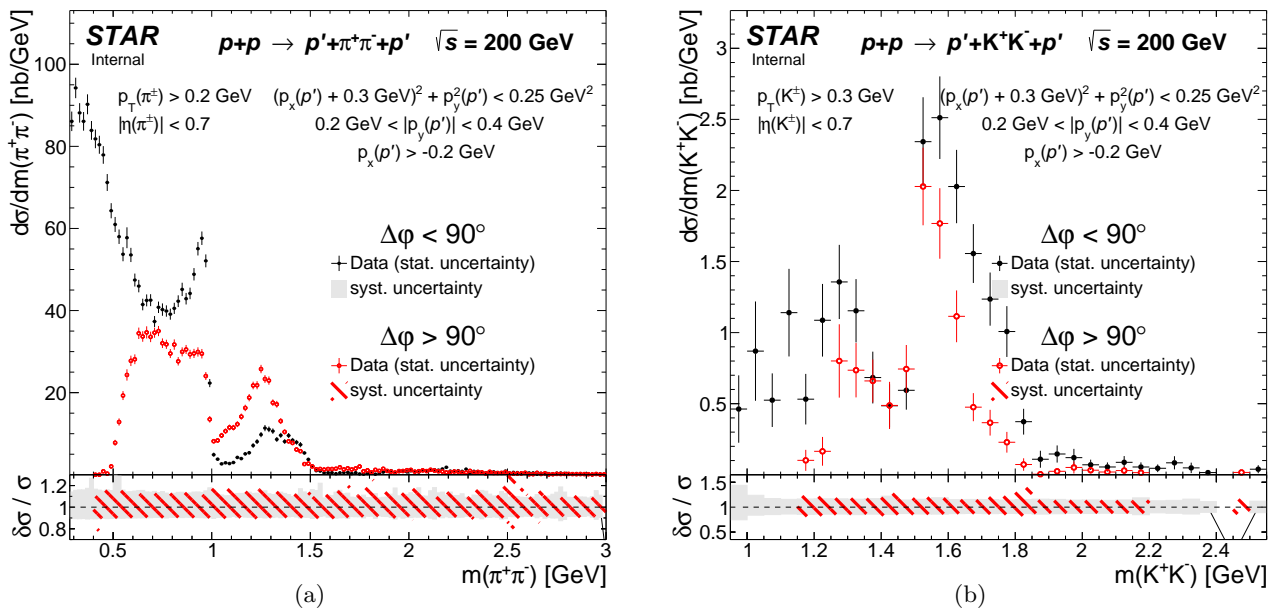


Figure 7.2

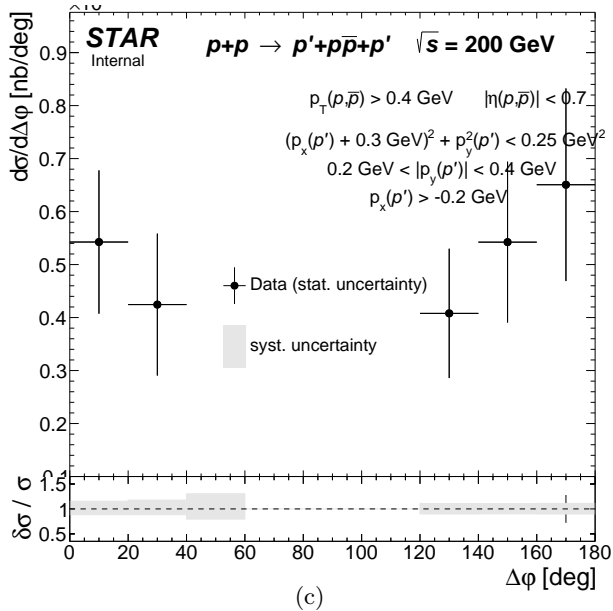
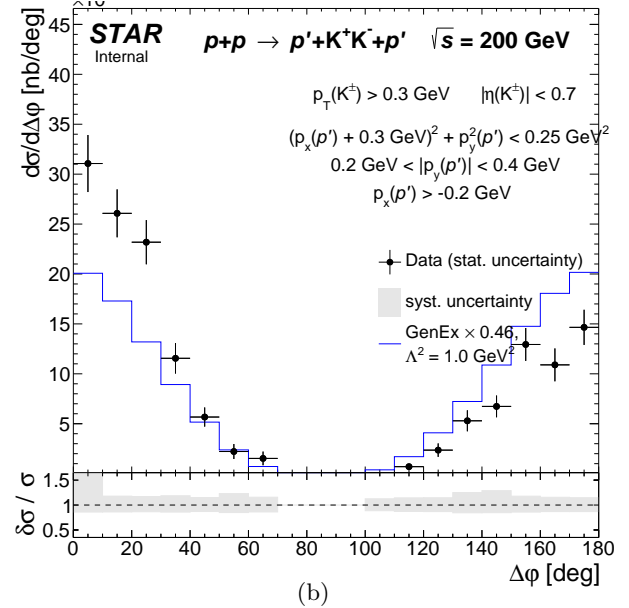
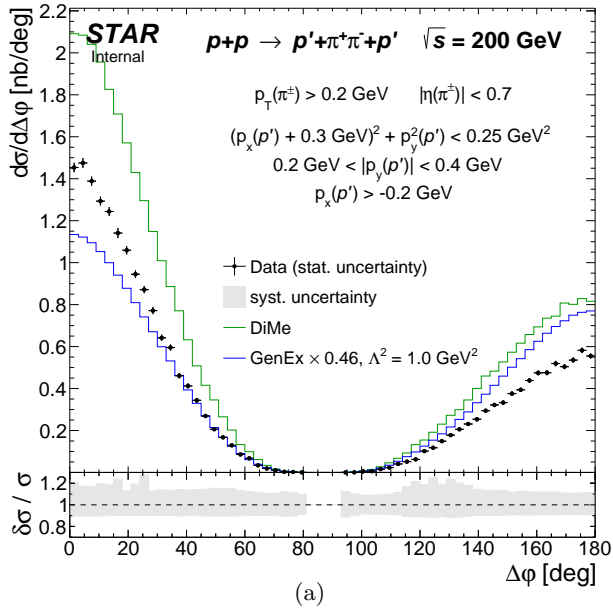


Figure 7.3

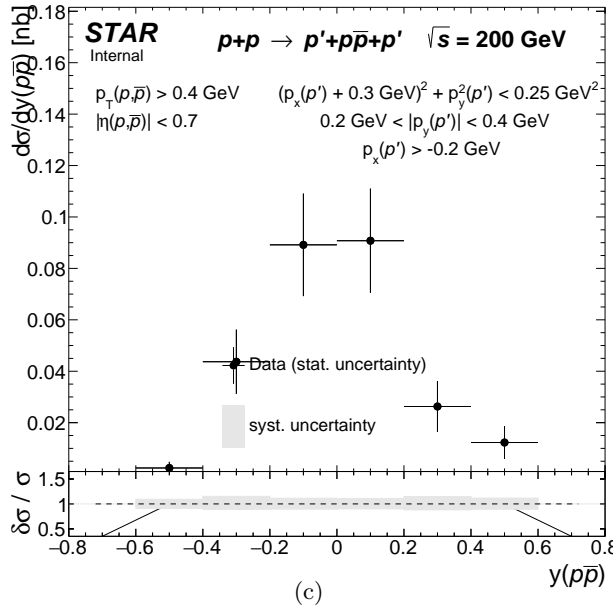
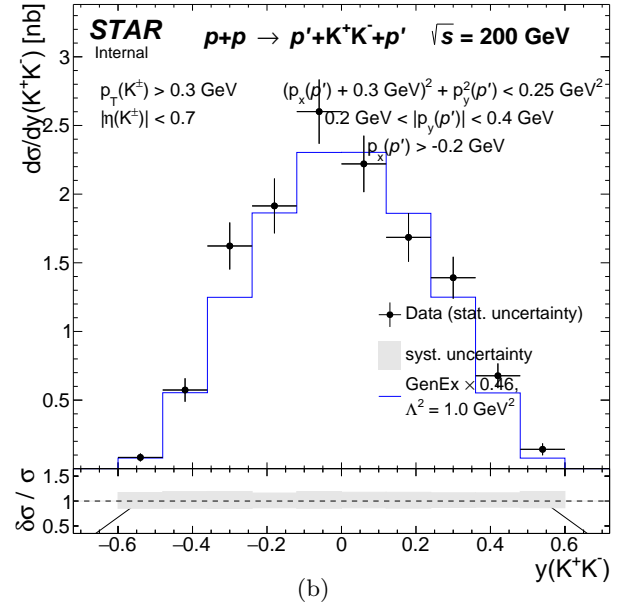
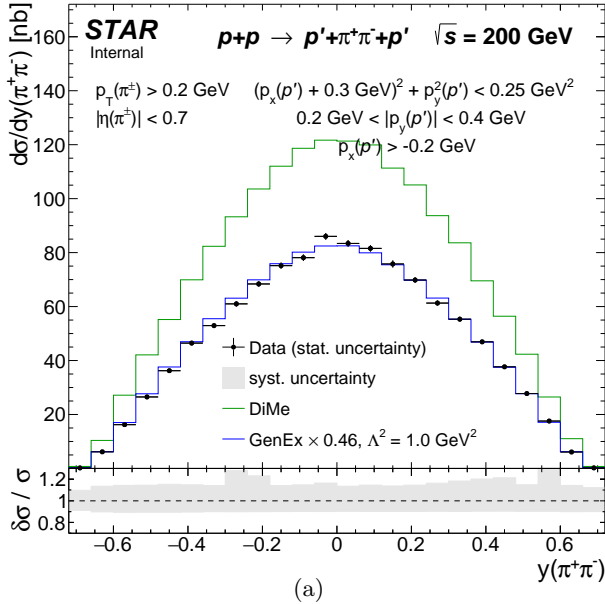


Figure 7.4

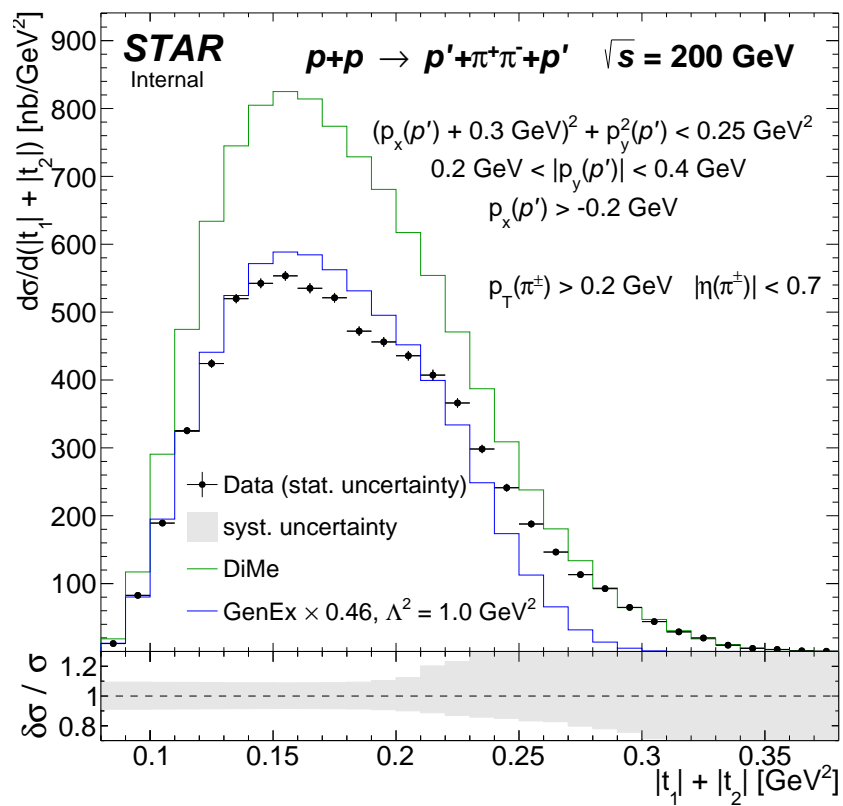
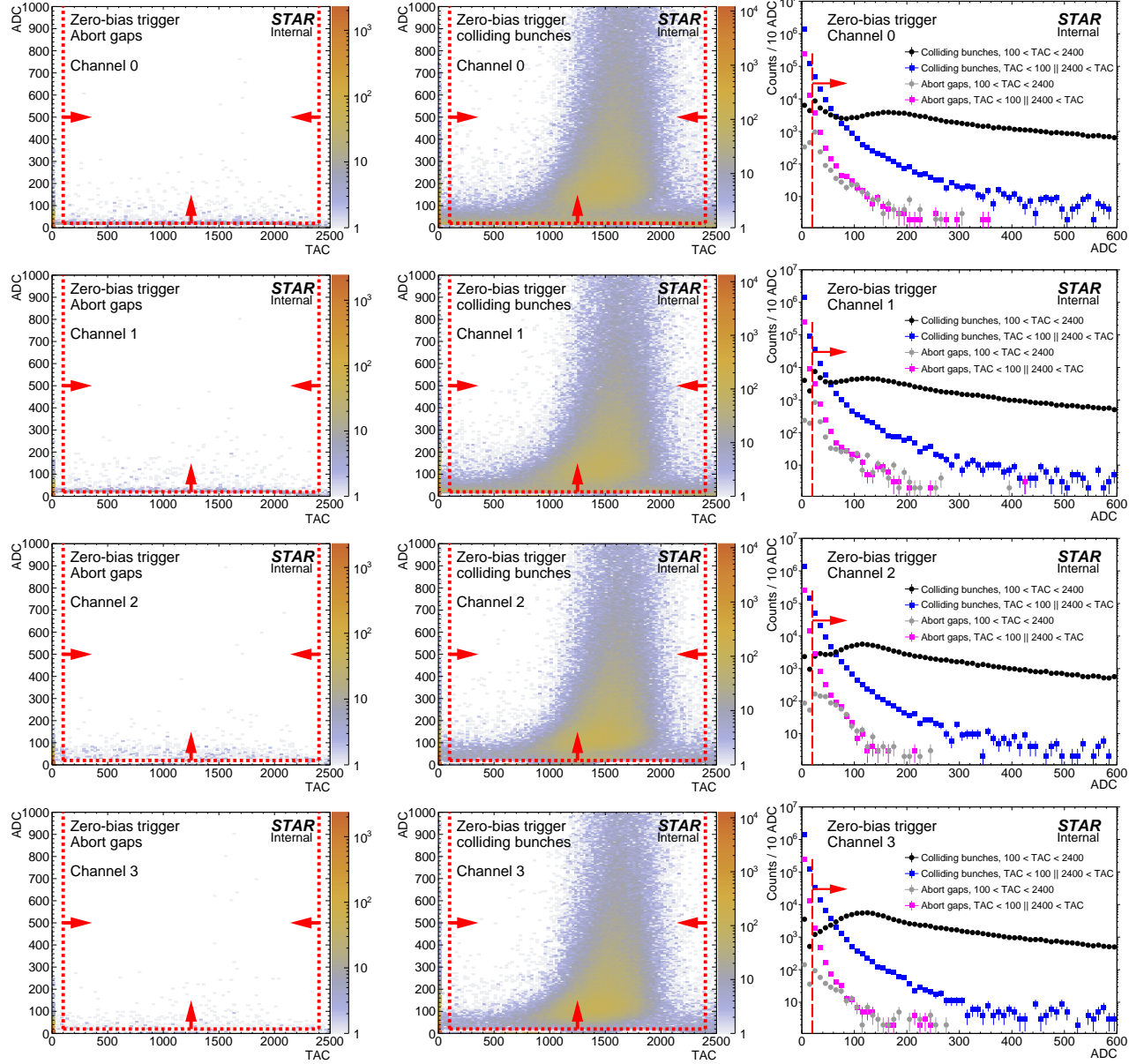
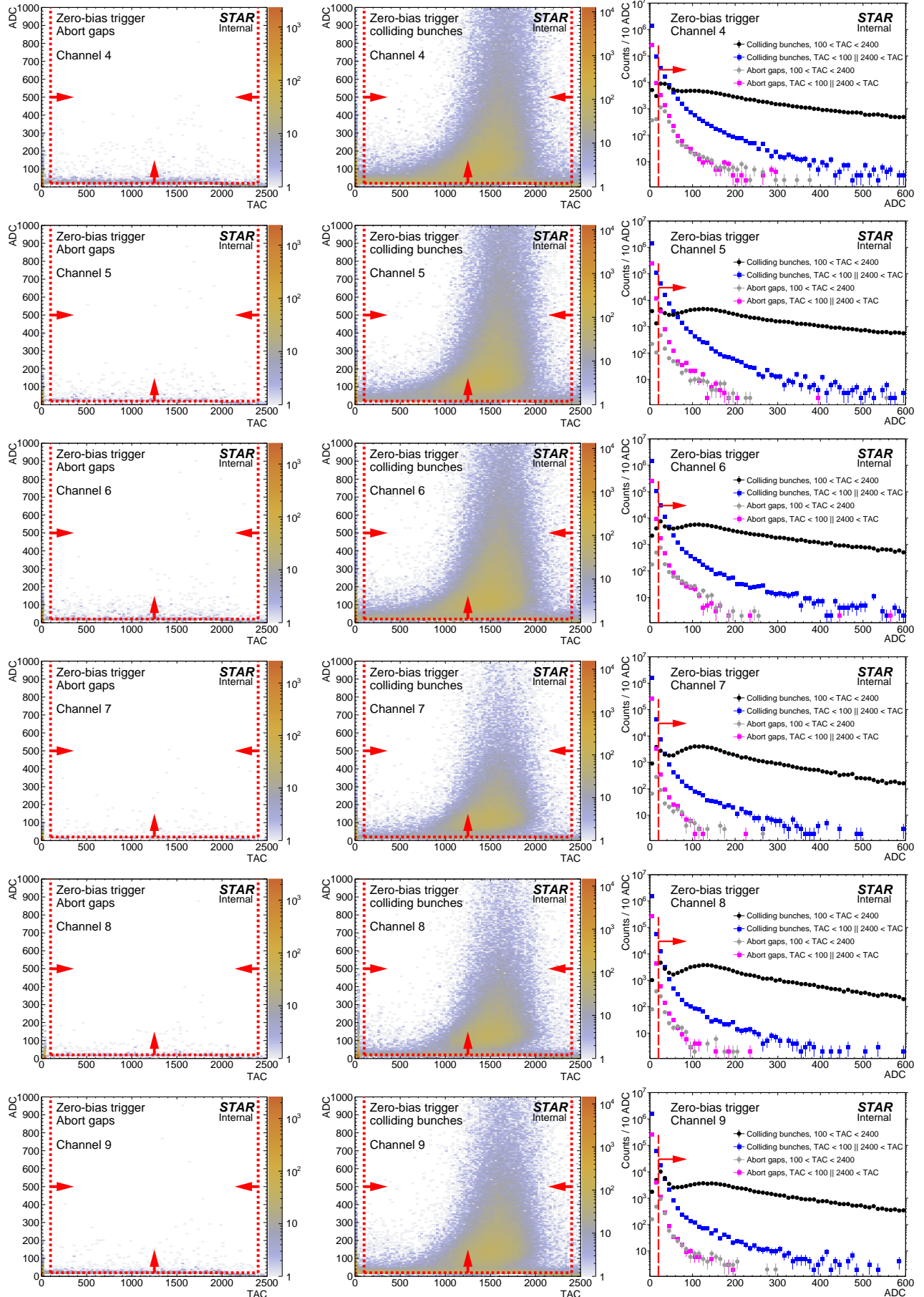


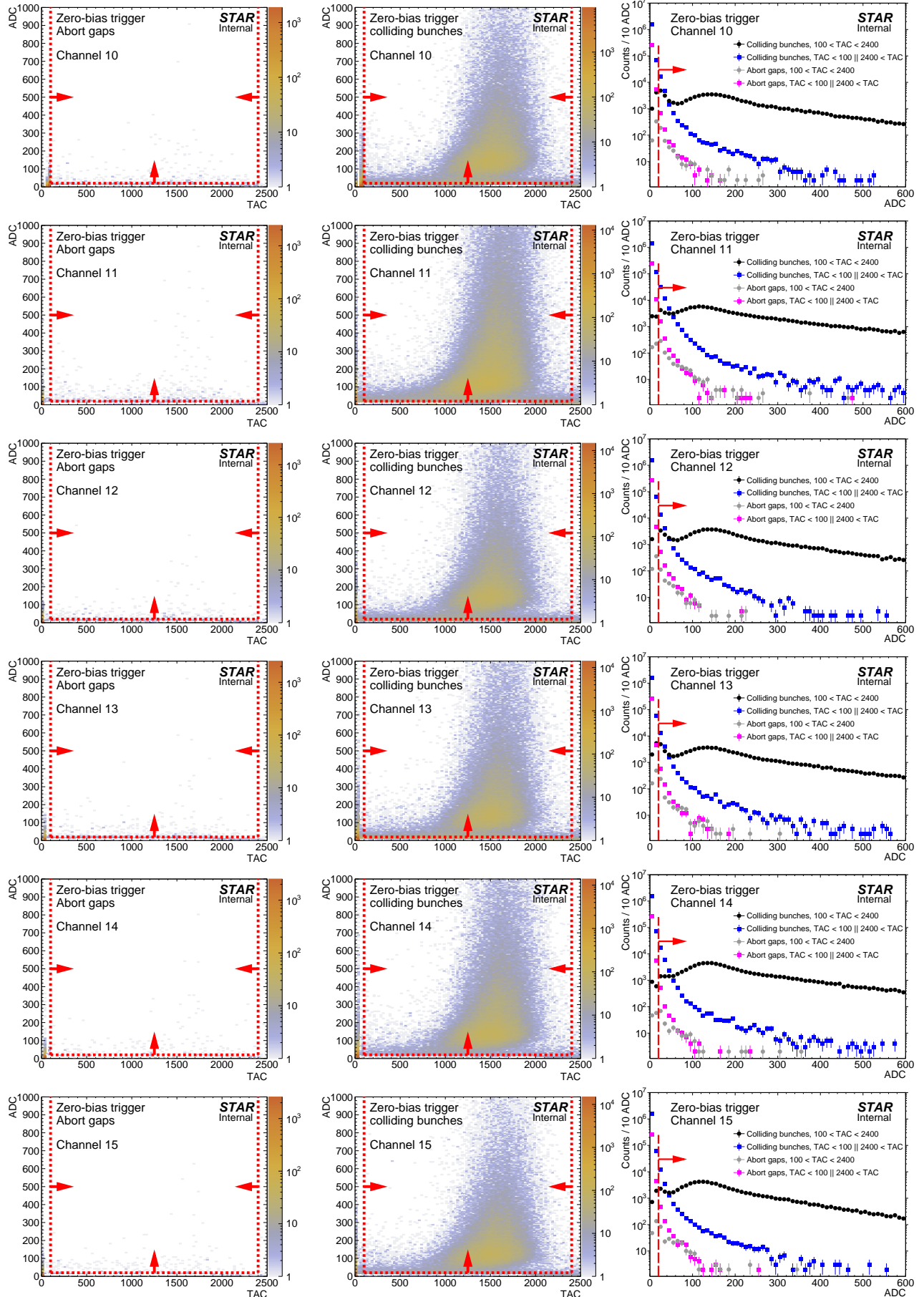
Figure 7.5: Cut flow.

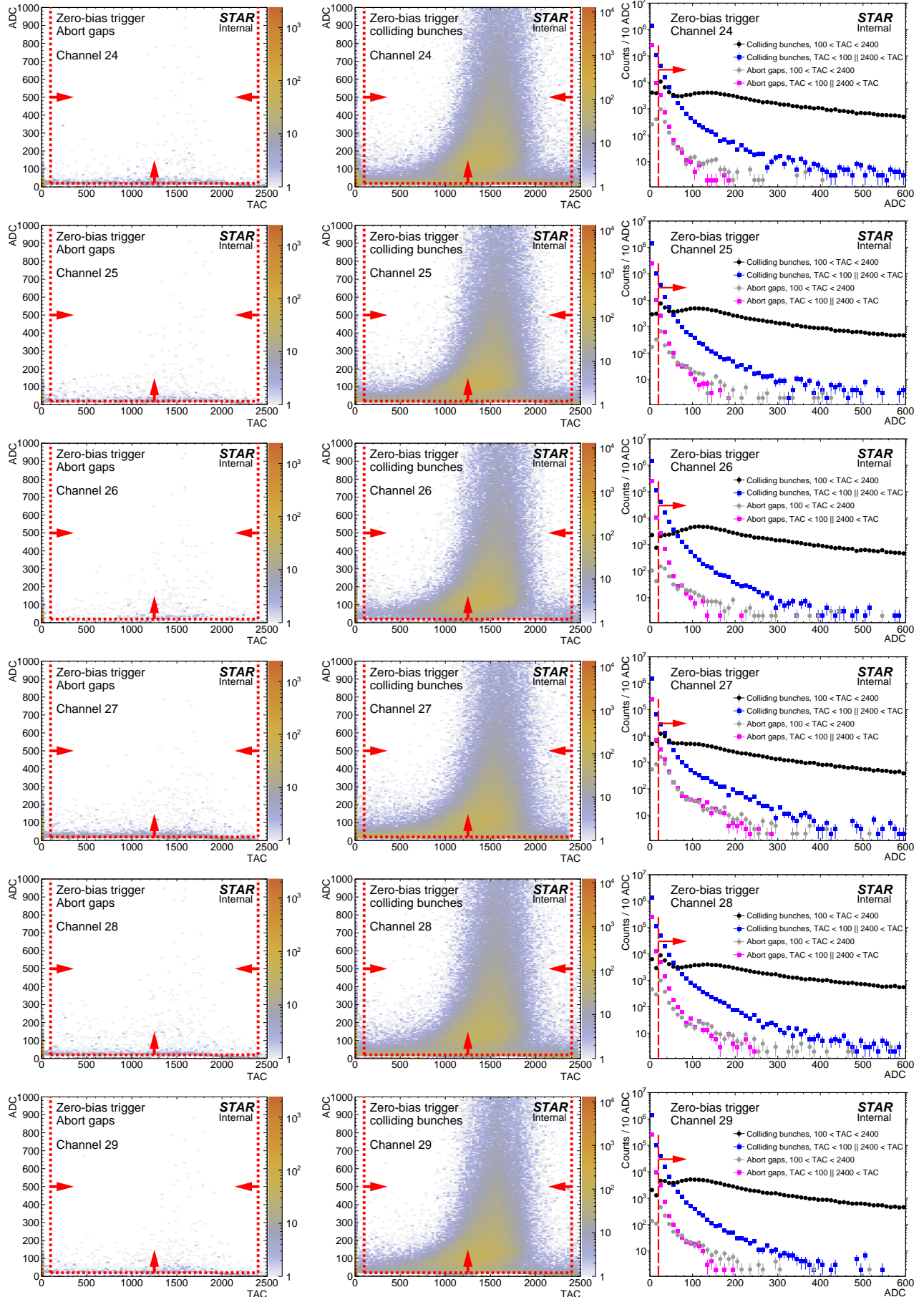
A. BBC response

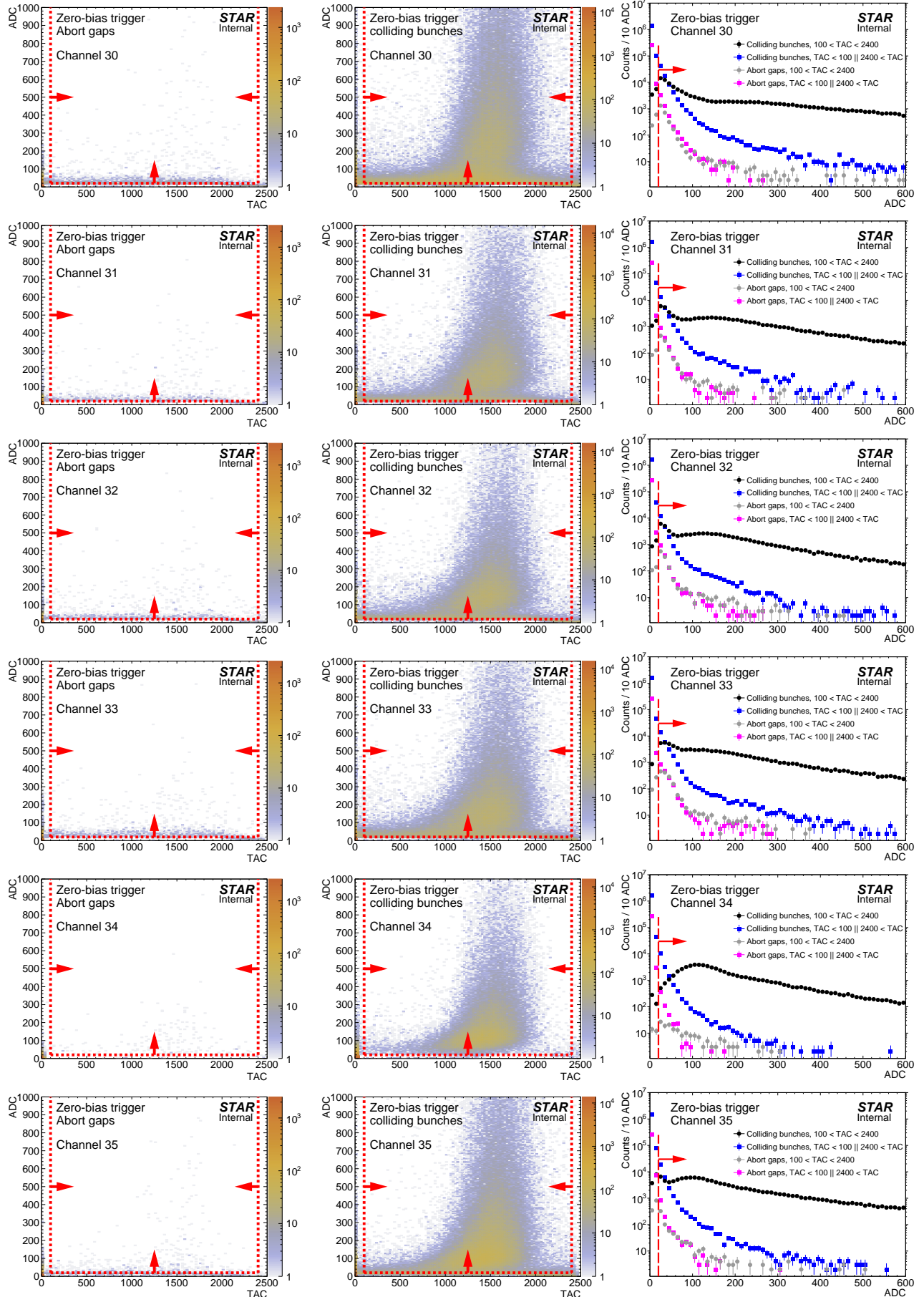
Figure A.1: Two-dimensional distribution of ADC vs. TAC counts per BBC-small channel in abort gaps (left) and colliding bunches (middle), and one-dimensional projection on x -axis (ADC) for selected ranges of TAC for colliding bunches and abort gaps (right). Each row represents single channel (small BBC tile). Red lines and arrows indicate thresholds for a signal in given channel.











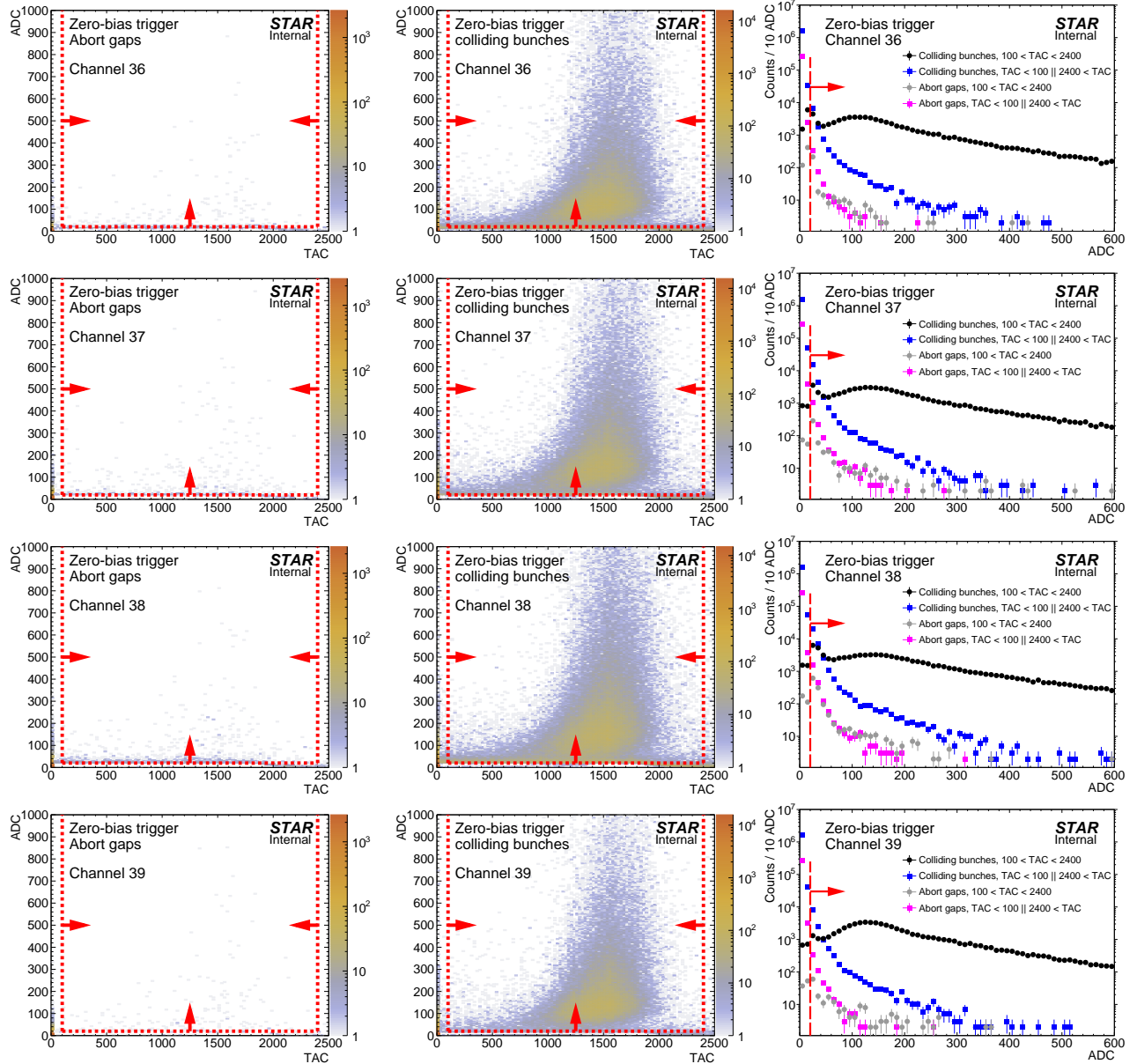
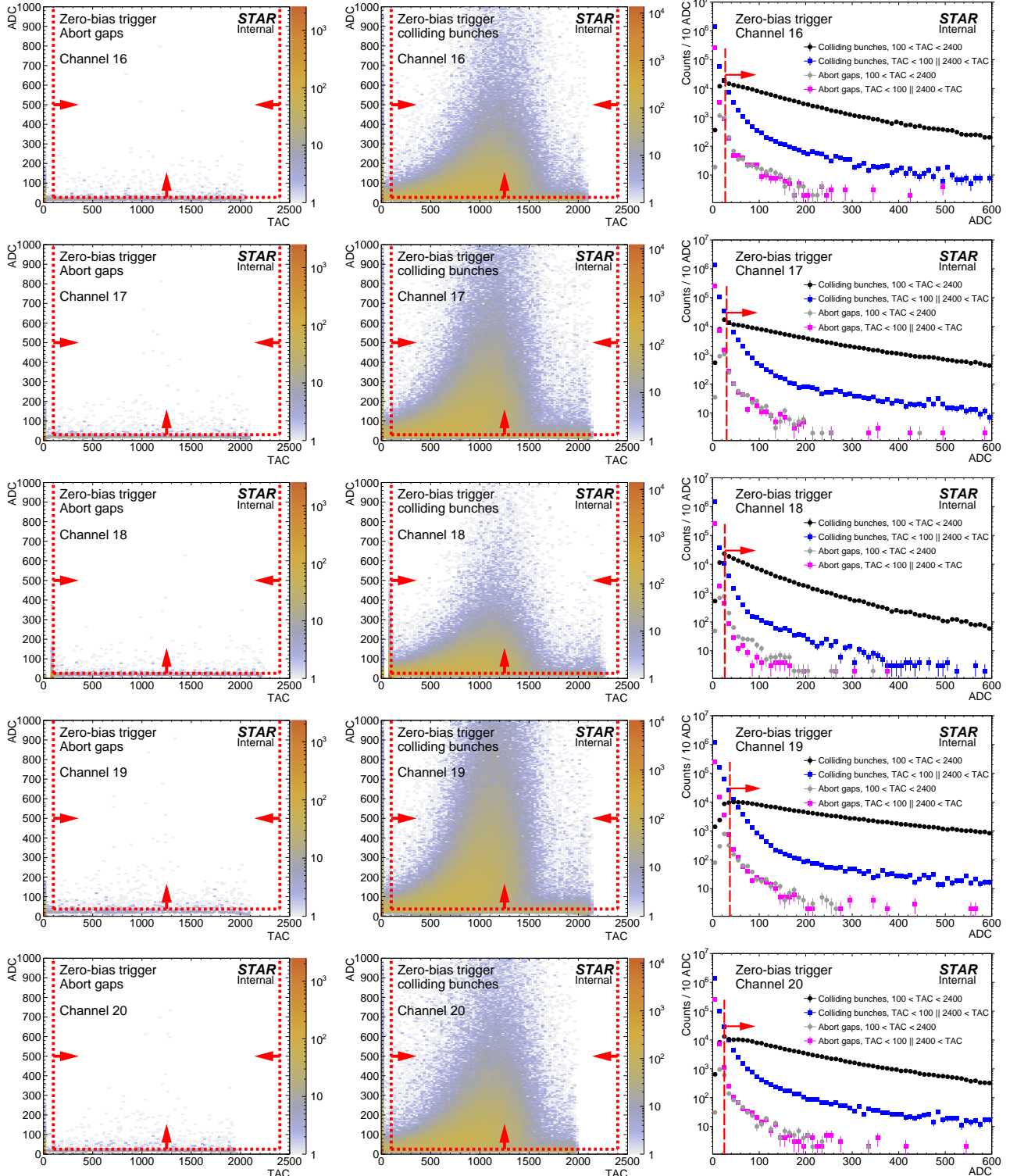
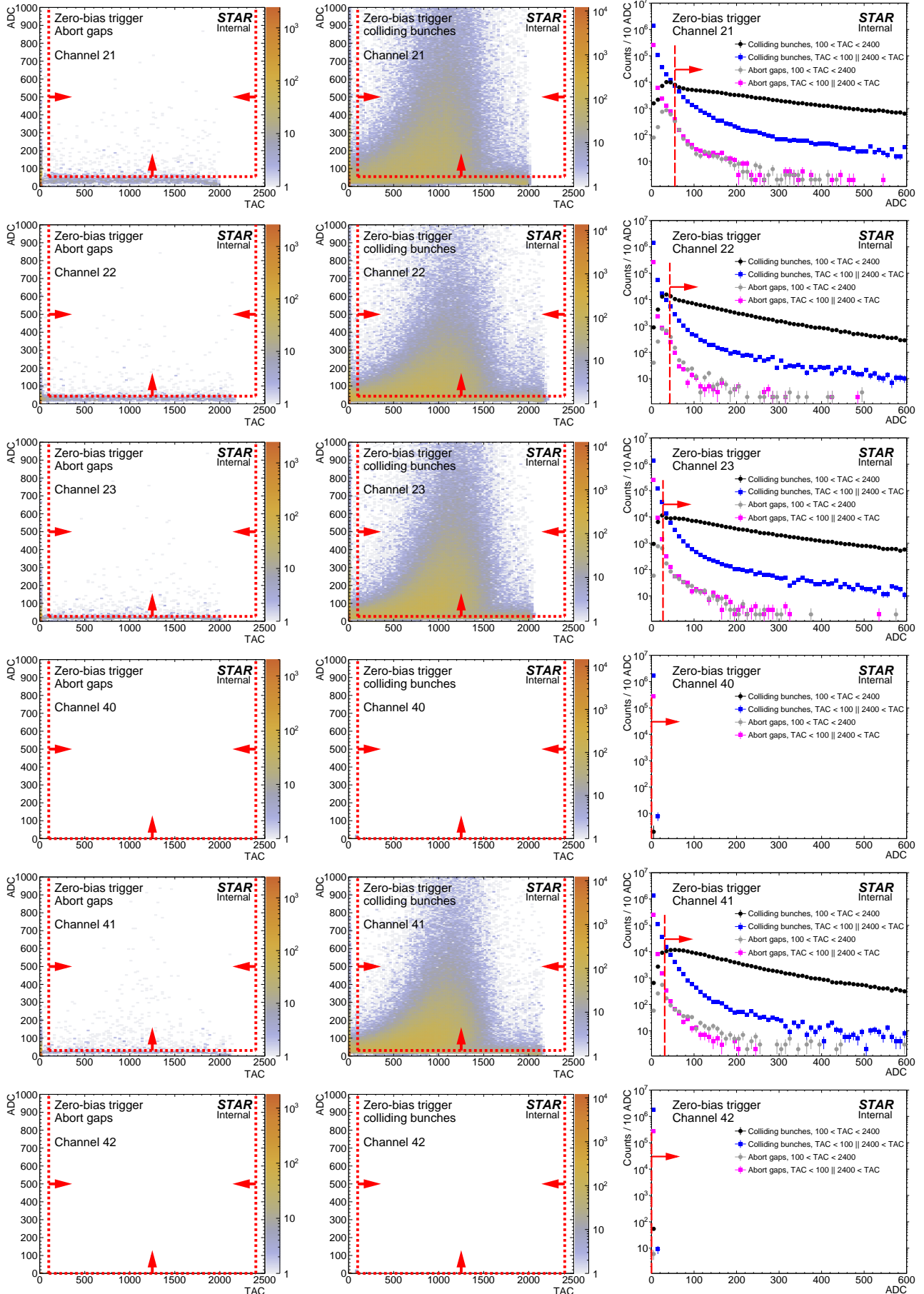
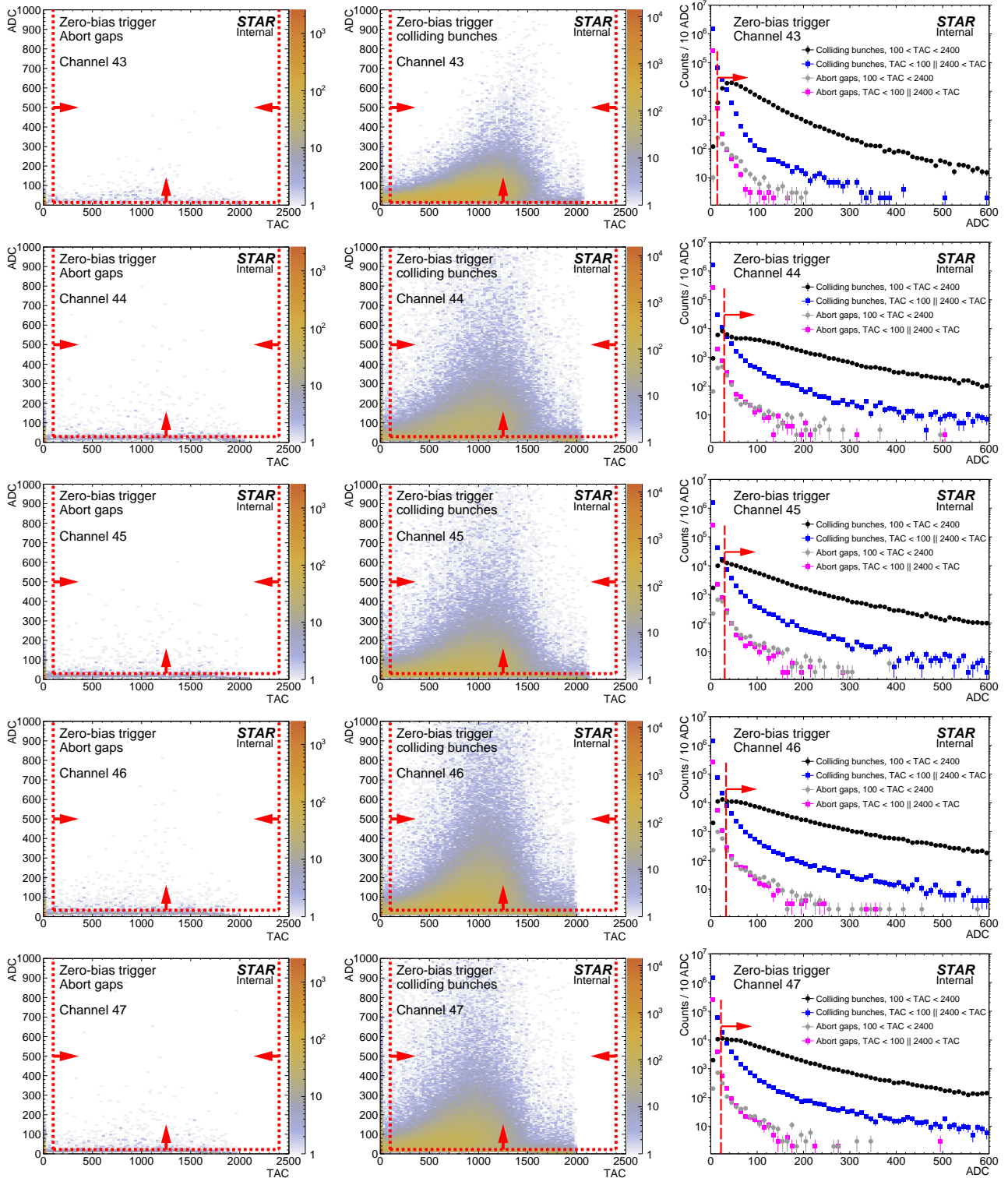


Figure A.2: Two-dimensional distribution of ADC vs. TAC counts per BBC-large channel in abort gaps (left) and colliding bunches (middle), and one-dimensional projection on x -axis (ADC) for selected ranges of TAC for colliding bunches and abort gaps (right). Each row represents single channel (large BBC tile). Red lines and arrows indicate thresholds for a signal in given channel.







B. Formulation of total RP efficiency

Definitions:

- RP^E - single good quality track (satisfying cuts C4.1-C4.2) on the east side,
- RP^W - single good quality track (satisfying cuts C4.1-C4.2) on the west side,
- TR^E - trigger signal in the RP branch with single good track on the east side,
- $TR^{\neq E}$ - trigger signal in the RP branch other than branch with single good track on the east side,
- TR^W - trigger signal in the RP branch with single good track on the west side,
- $TR^{\neq W}$ - trigger signal in the RP branch other than branch with single good track on the west side,
- $Veto$ - trigger veto on the simultaneous trigger signal in Up and Down RPs (ET&IT),
- $Veto^{PU}$ - trigger veto on ET&IT (Veto) due to pile-up interactions,
- $Veto^{DM}$ - trigger veto on ET&IT (Veto) due to forward proton interaction with dead material.

The total efficiency related to both east and west forward protons in CEP event has the following form:

$$\mathcal{E}(RP^E \wedge RP^W \wedge TR^E \wedge TR^W \wedge !Veto) = \mathcal{E}(RP^E \wedge RP^W | TR^E \wedge TR^W \wedge !Veto) \times \mathcal{E}(TR^E \wedge TR^W \wedge !Veto), \quad (B.1)$$

where the r.h.s. part of the equation is factorized using the rules of conditional probability to two components describing reconstruction and selection efficiency (first) and trigger efficiency (second).

The reconstruction and selection efficiency part can be represented as a product of single-proton reconstruction and selection efficiencies described in Sec. 4.2.3 with an additional scaling factor in the denominator:

$$\mathcal{E}(RP^E \wedge RP^W | TR^E \wedge TR^W \wedge !Veto) = \frac{\mathcal{E}(RP^E | TR^E \wedge !TR^{\neq E}) \times \mathcal{E}(RP^W | TR^W \wedge !TR^{\neq W})}{1 - \mathcal{E}(!RP^E \wedge !RP^W | TR^E \wedge TR^W \wedge !Veto)} \quad (B.2)$$

This denominator accounts for the fact that the efficiencies of the east and west RPs are correlated. To be more precise, unsuccessful reconstruction/selection of RP track on the east and west side in the same event can be a result of a pile-up interaction, typically of elastic proton-proton scattering, producing additional tracks/showers simultaneously in east and west RPs and thus introducing simultaneous east and west RP inefficiency. Without this factor the sole product of east and west efficiencies would account for discussed inefficiency twice - the total RP efficiency would be then underestimated. The effect is small (as can be read from Fig. 4.5), but we correct for it for completeness.

In the component of RP efficiency related to the trigger we can use again the conditional probability and factorize it to part connected with the trigger veto (first) and the efficiency of detecting a signal of both forward protons by the trigger system (second):

$$\mathcal{E}(TR^E \wedge TR^W \wedge !Veto) = \mathcal{E}(!Veto | TR^E \wedge TR^W) \times \mathcal{E}(TR^E \wedge TR^W). \quad (B.3)$$

Efficiency of the triggering $\mathcal{E}(TR^E \wedge TR^W)$ is basically 1. Efficiency of the (lack of) veto if forward protons are triggering in east and west RPs can be decomposed to efficiency of the veto induced by the pile-up interaction in the same bunch crossing ($Veto^{PU}$) and efficiency of the veto induced by the interaction of the CEP protons with the material of the accelerator and detectors ($Veto^{DM}$):

$$\begin{aligned} \mathcal{E}(!Veto | TR^E \wedge TR^W) &= \left| Veto = Veto^{PU} \vee Veto^{DM} \right| = \mathcal{E}(!Veto^{PU} \wedge !Veto^{DM} | TR^E \wedge TR^W) = \\ &= \mathcal{E}(!Veto^{DM} | !Veto^{PU} \wedge TR^E \wedge TR^W) \times \mathcal{E}(!Veto^{PU} | TR^E \wedge TR^W). \end{aligned} \quad (B.4)$$

The first term of the last part of Eq. (B.4) described in Sec. 4.2.1.2 can be safely factorized as the probability of veto induced by the primary CEP proton on the east side is totally independent from the similar probability on the west side:

$$\begin{aligned} \mathcal{E}(!Veto^{DM} | !Veto^{PU} \wedge TR^E \wedge TR^W) &= \\ &= \mathcal{E}^E(!Veto^{DM} | !Veto^{PU} \wedge TR^E \wedge TR^W) \times \mathcal{E}^W(!Veto^{DM} | !Veto^{PU} \wedge TR^E \wedge TR^W) \end{aligned} \quad (B.5)$$

The second term of the last part of Eq. (B.4) related with the pile-up is incorporated to overall efficiency of online and offline vetoes described in Sec. 4.2.2.3 - this is required by the correlation of vetoes, the possibility that vetoes in independent subdetectors take place in the same bunch crossing. This could happen if e.g. single diffraction event occurs on top of the CEP event, yielding a BBC signal and RP signal, both vetoing RP_CPT2 trigger.

C. Reconstruction of m_{TOF}^2

Definitions:

- t_0 - time of the primary pp interaction
- $t_{1,2}$ - time of detection of the hit in TOF by particle 1(2)
- $L_{1,2}$ - helical path of the particle 1(2) from the interaction vertex to the TOF cell with reconstructed hit,
- $p_{1,2}$ - magnitude of momentum of particle 1(2),
- $m_{1,2}$ - mass of particle 1(2),

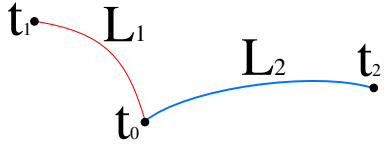


Figure C.1: Scheme of two central tracks of lengths L_1 and L_2 , produced in common vertex in moment t_0 , hitting cells in TOF detector in moments t_1 and t_2 .

From the simple algebra below which describes relation between track lengths, momenta and times of hit detection one can derive formula for the squared mass of two particles, assuming that their masses are equal (particles are of the same type).

Below we assume $c = 1$. We can write a set of two equations connecting the time that it takes for each particle to reach the TOF, starting from the interaction vertex:

$$\begin{cases} t_1 - t_0 = L_1 \sqrt{1 + \frac{m_1^2}{p_1^2}}, \\ t_2 - t_0 = L_2 \sqrt{1 + \frac{m_2^2}{p_2^2}}. \end{cases} \quad (\text{C.1})$$

By adding the two equations above we get

$$\Delta t = t_1 - t_2 = L_1 \sqrt{1 + \frac{m_1^2}{p_1^2}} - L_2 \sqrt{1 + \frac{m_2^2}{p_2^2}}. \quad (\text{C.2})$$

In CEP of two opposite-sign particles always the same species of particles are produced, therefore

$$m_1 = m_2 = m. \quad (\text{C.3})$$

If we substitute m_1 and m_2 with m in Eq. (C.2) and transform the equation to remove the square roots we get a quadratic equation of the form

$$\mathcal{A} \times (m_{\text{TOF}}^2)^2 + \mathcal{B} \times m_{\text{TOF}}^2 + \mathcal{C} = 0. \quad (\text{C.4})$$

Parameters of the Eq. (C.4) are given below:

$$\mathcal{A} = -2 \frac{L_1^2 L_2^2}{p_1^2 p_2^2} + \frac{L_1^4}{p_1^4} + \frac{L_2^4}{p_2^4}, \quad (\text{C.5})$$

$$\mathcal{B} = -2 L_1^2 L_2^2 \left(\frac{1}{p_1^2} + \frac{1}{p_2^2} \right) + \frac{2 L_1^4}{p_1^2} + \frac{2 L_2^4}{p_2^2} - 2 (\Delta t)^2 \left(\frac{L_1^2}{p_1^2} + \frac{L_2^2}{p_2^2} \right), \quad (\text{C.6})$$

$$\mathcal{C} = (\Delta t)^4 - 2 (\Delta t)^2 (L_1^2 + L_2^2) + L_1^4 + L_2^4 - 2 L_1^2 L_2^2, \quad (\text{C.7})$$

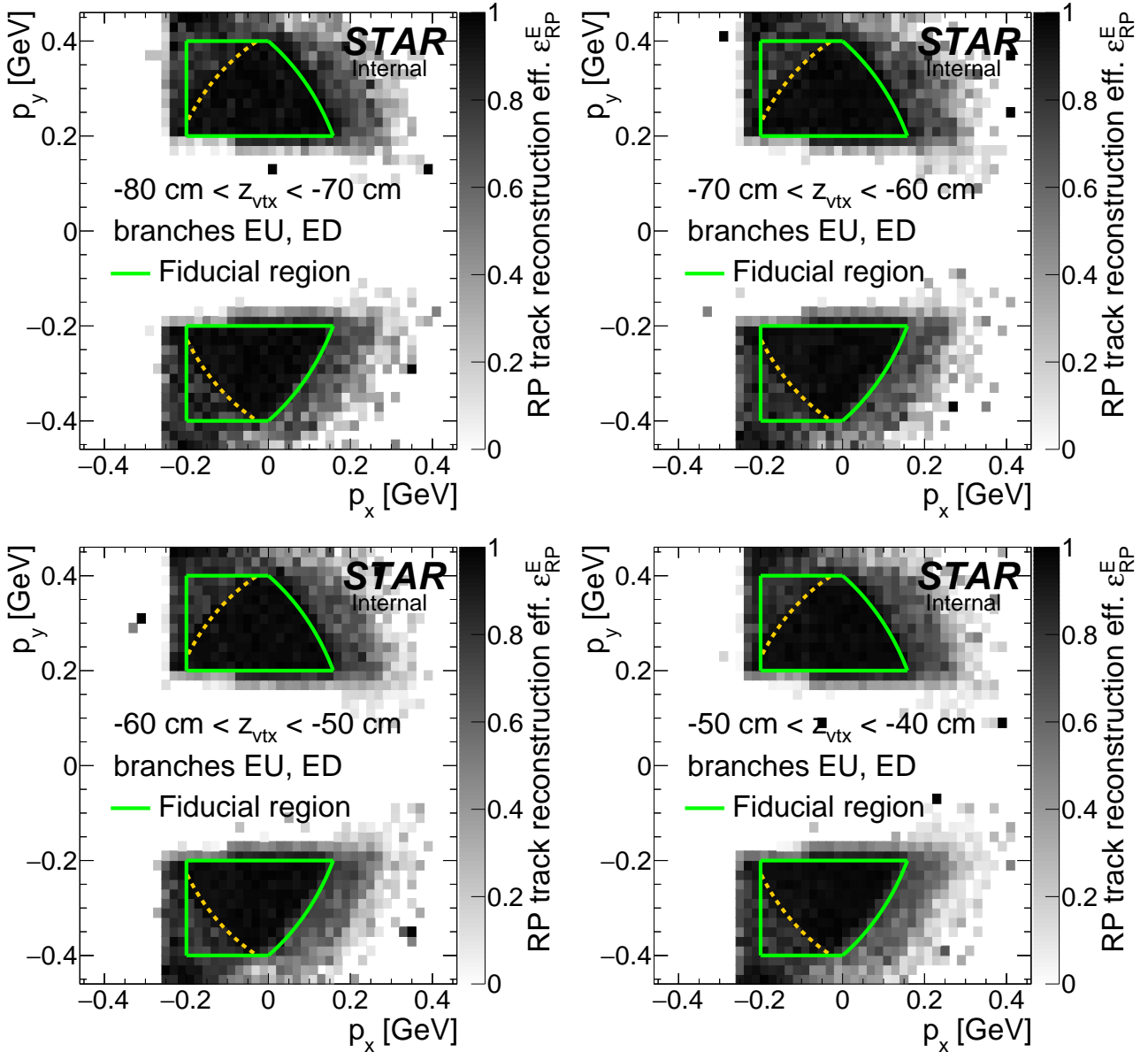
together with the final formula for a physical root of the quadratic equation which is used in the m_{TOF}^2 reconstruction:

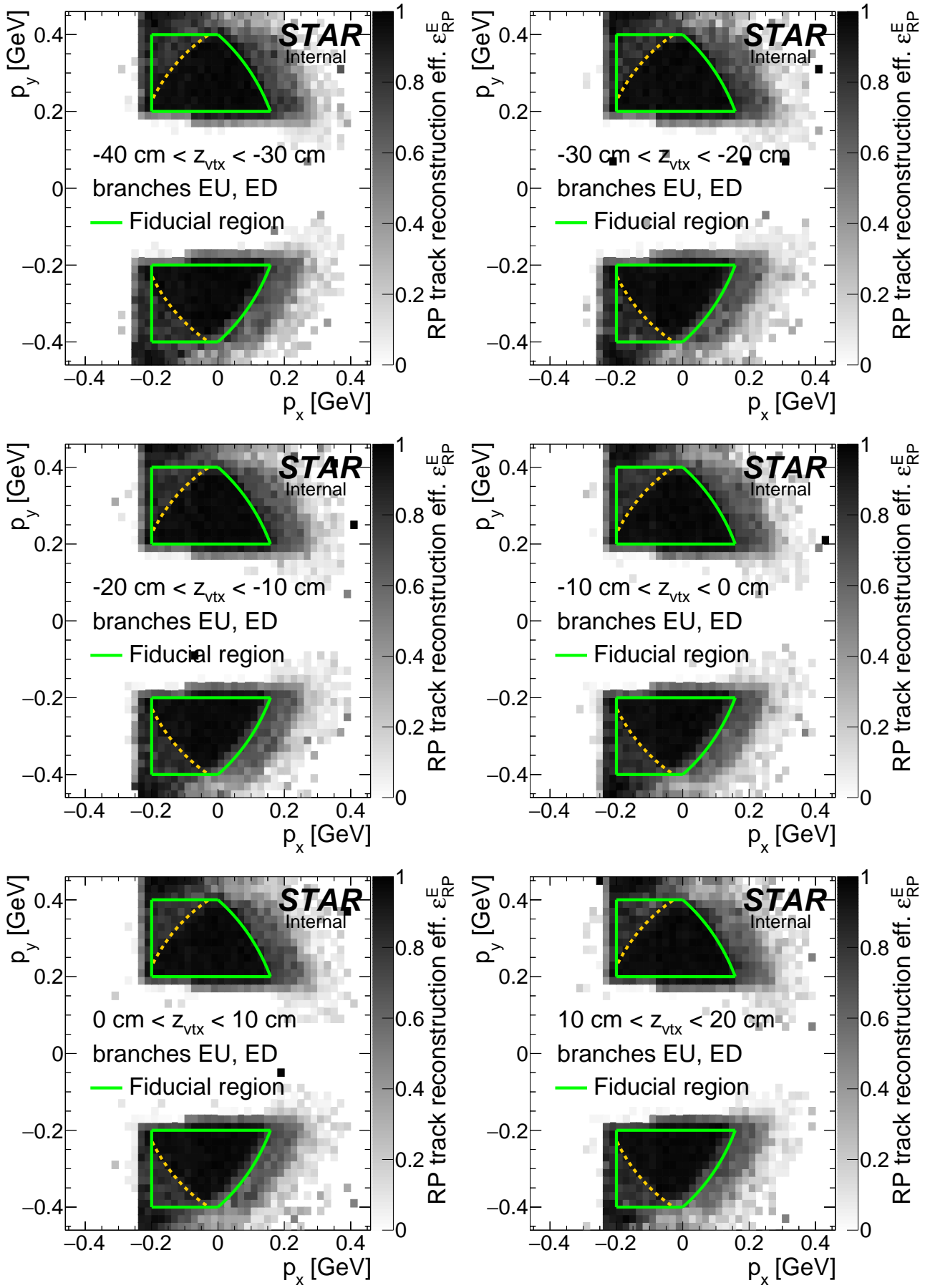
$$m_{\text{TOF}}^2 = \frac{-\mathcal{B} + \sqrt{\mathcal{B}^2 - 4\mathcal{A}\mathcal{C}}}{2\mathcal{A}}. \quad (\text{C.8})$$

D. RP efficiency

D.1 RP track acceptance, reconstruction and selection efficiency

Figure D.1: RP track acceptance, reconstruction and selection efficiency on the east side obtained from MC simulation embedded into zero-bias data. Each plot corresponds to z -vertex range given in the plot.





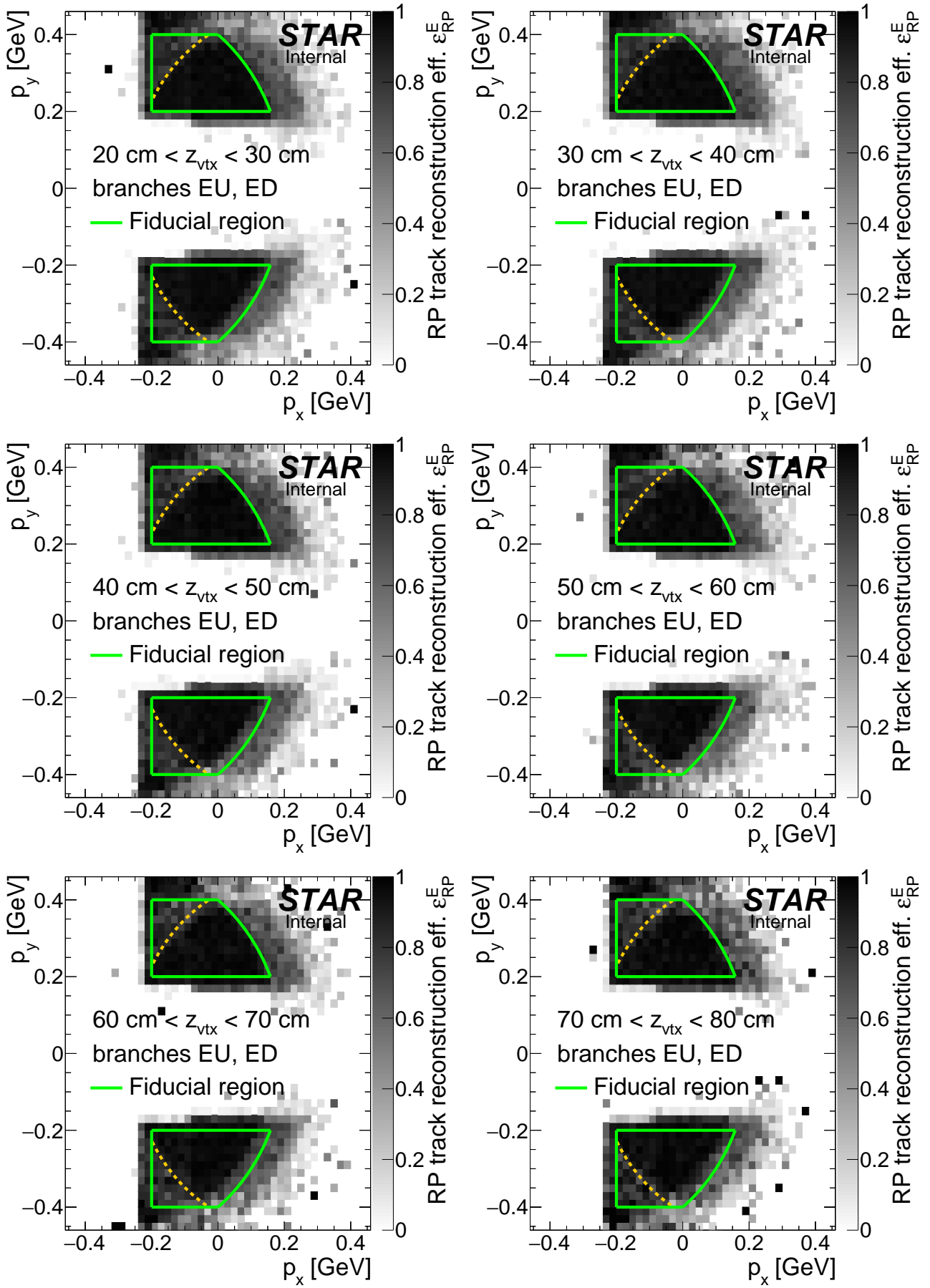
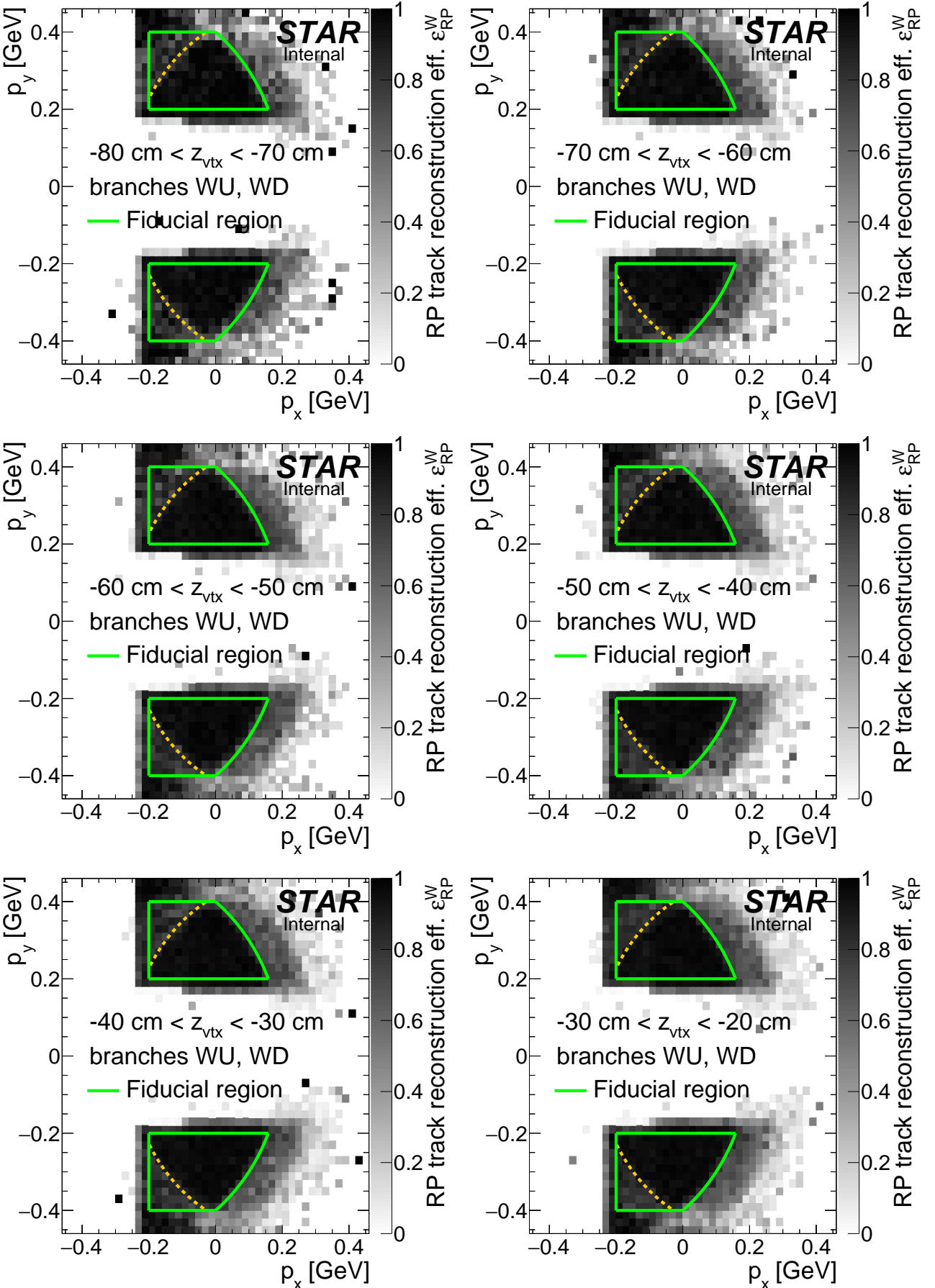
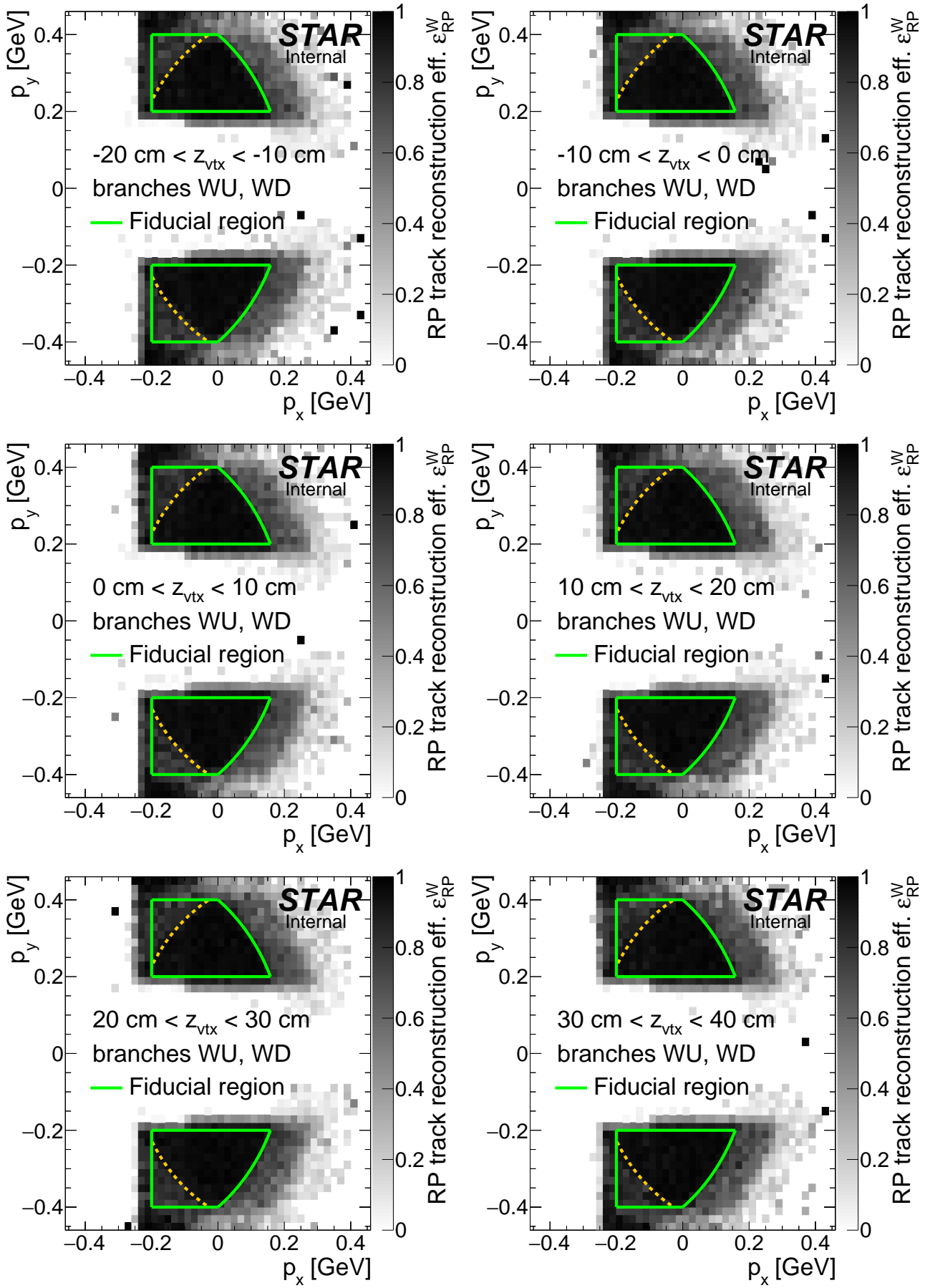
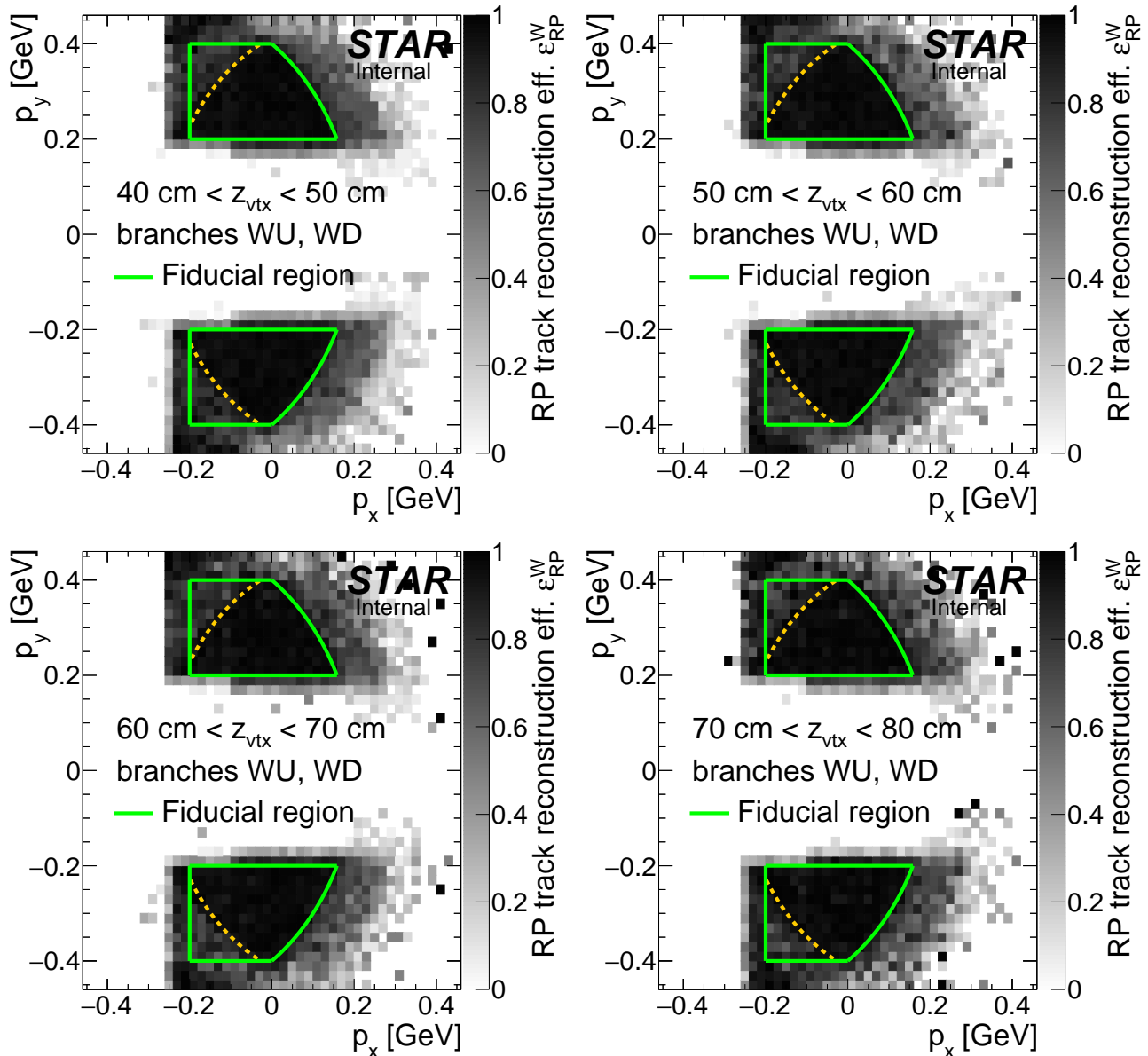


Figure D.2: RP track acceptance, reconstruction and selection efficiency on the west side obtained from MC simulation embedded into zero-bias data. Each plot corresponds to z -vertex range given in the plot.

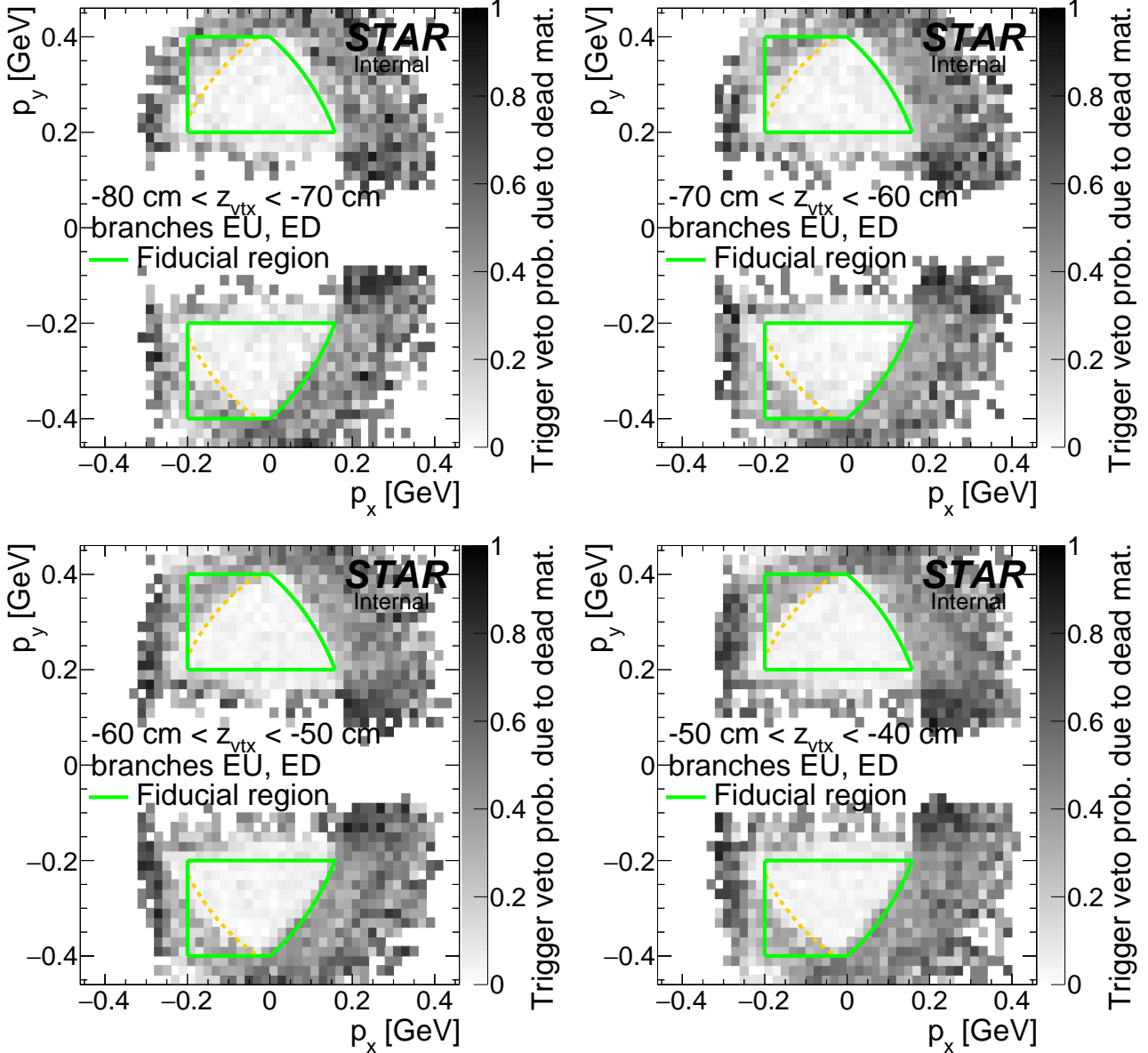


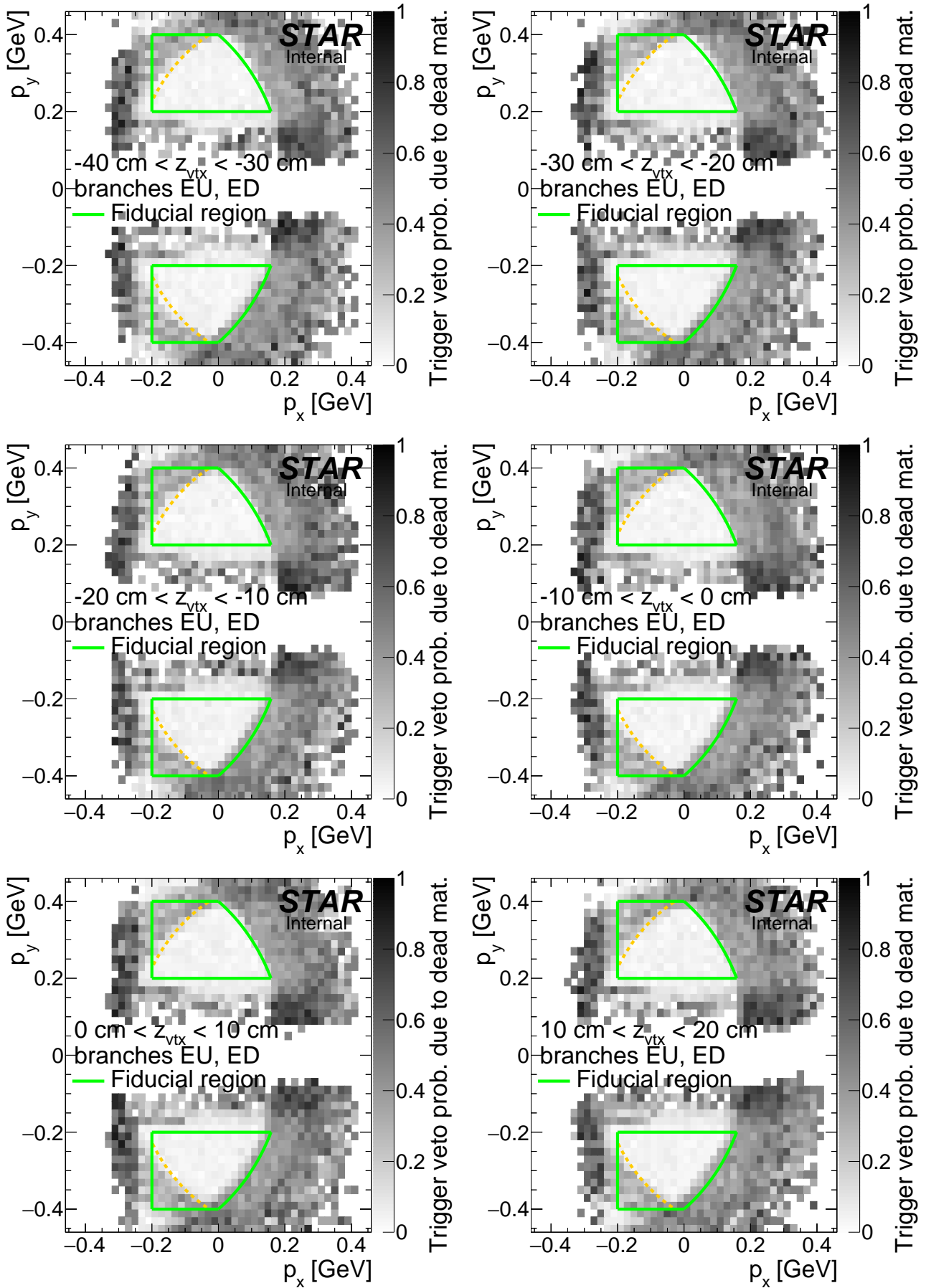




D.2 RP trigger veto probability related to dead material

Figure D.3: Probability of ET&IT trigger veto due to forward proton interaction with dead material on the east side. Results were obtained from forward proton MC simulation embedded into zero-bias data. Each plot corresponds to z -vertex range given in the plot.





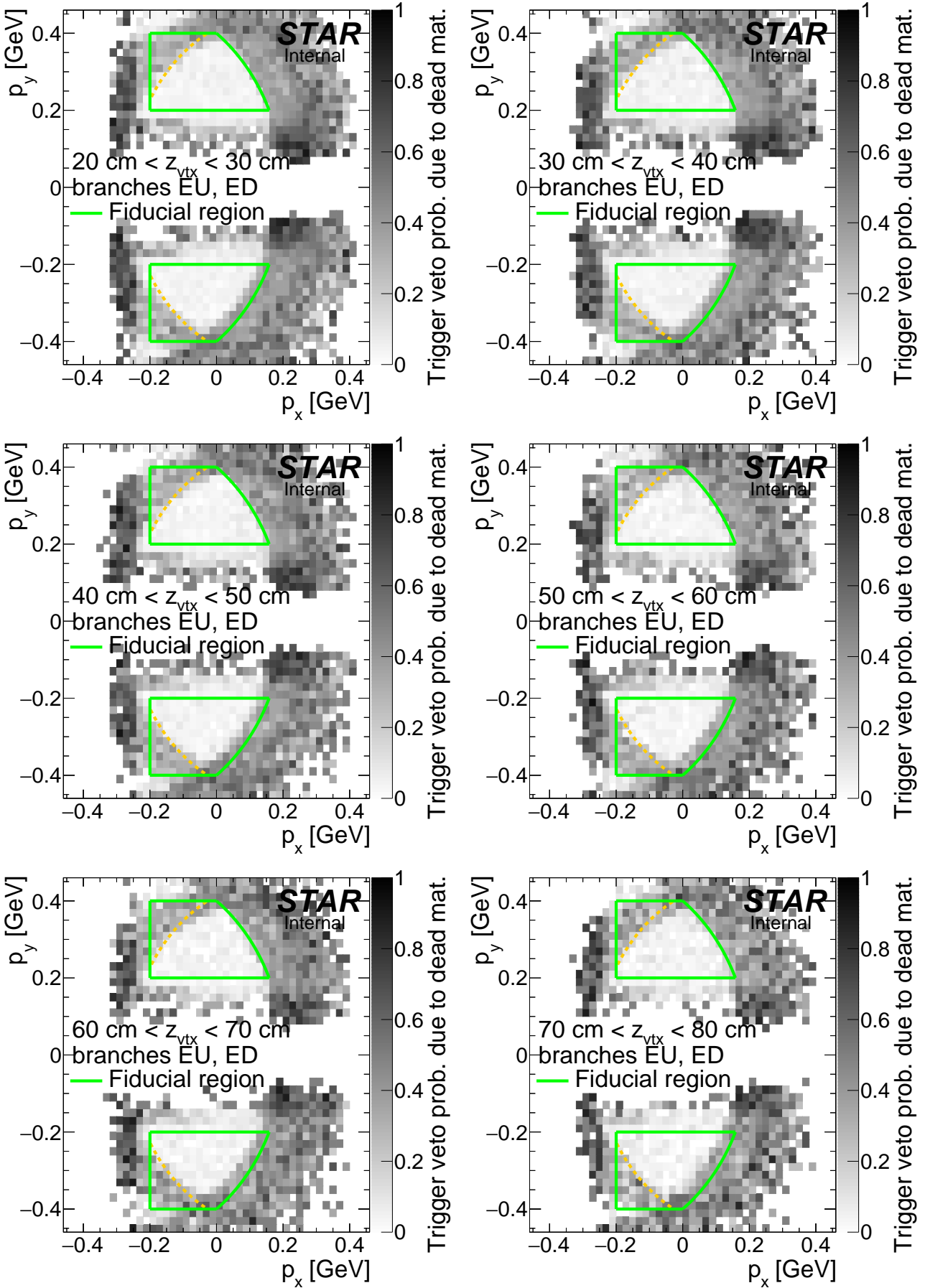
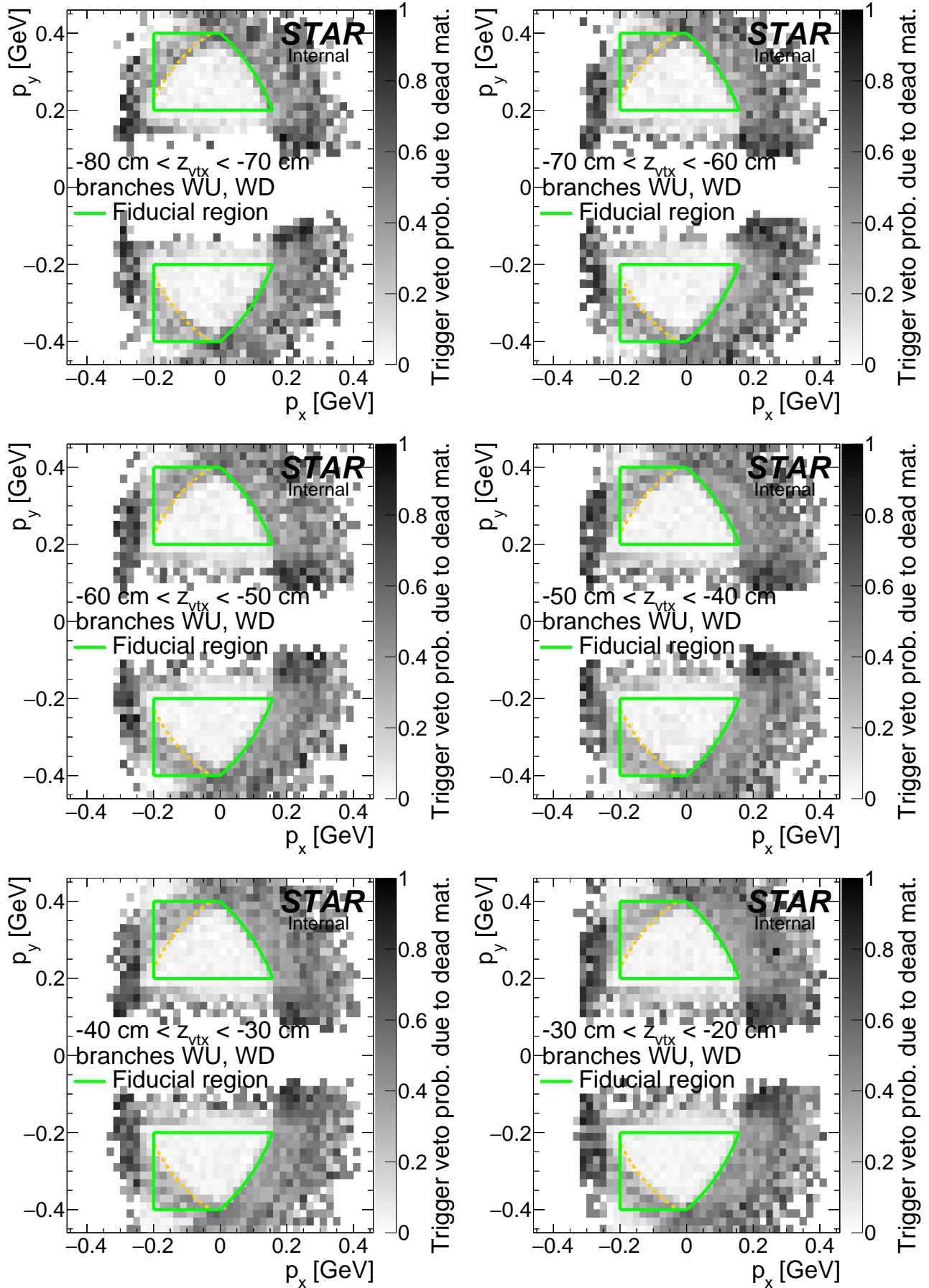
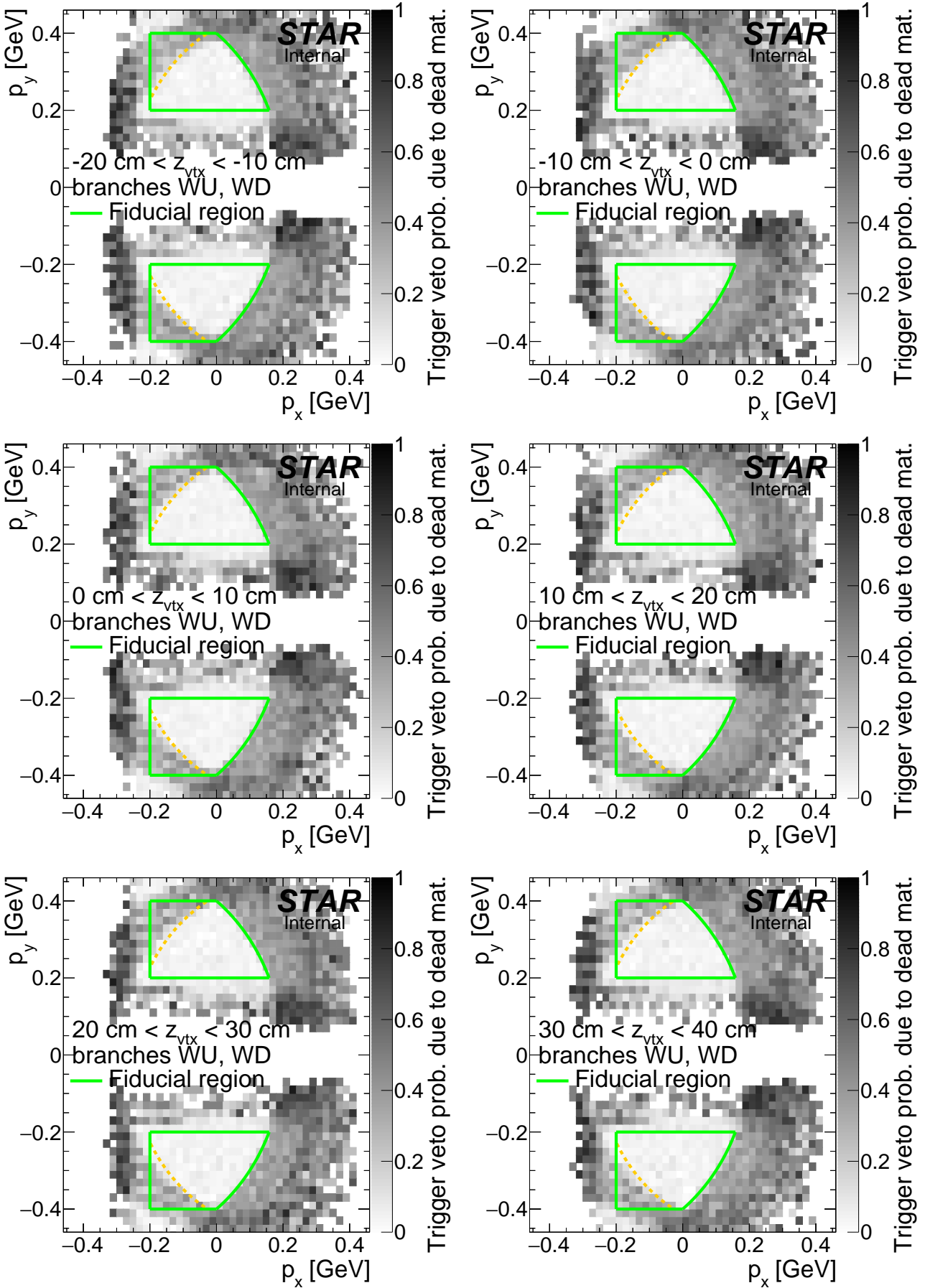
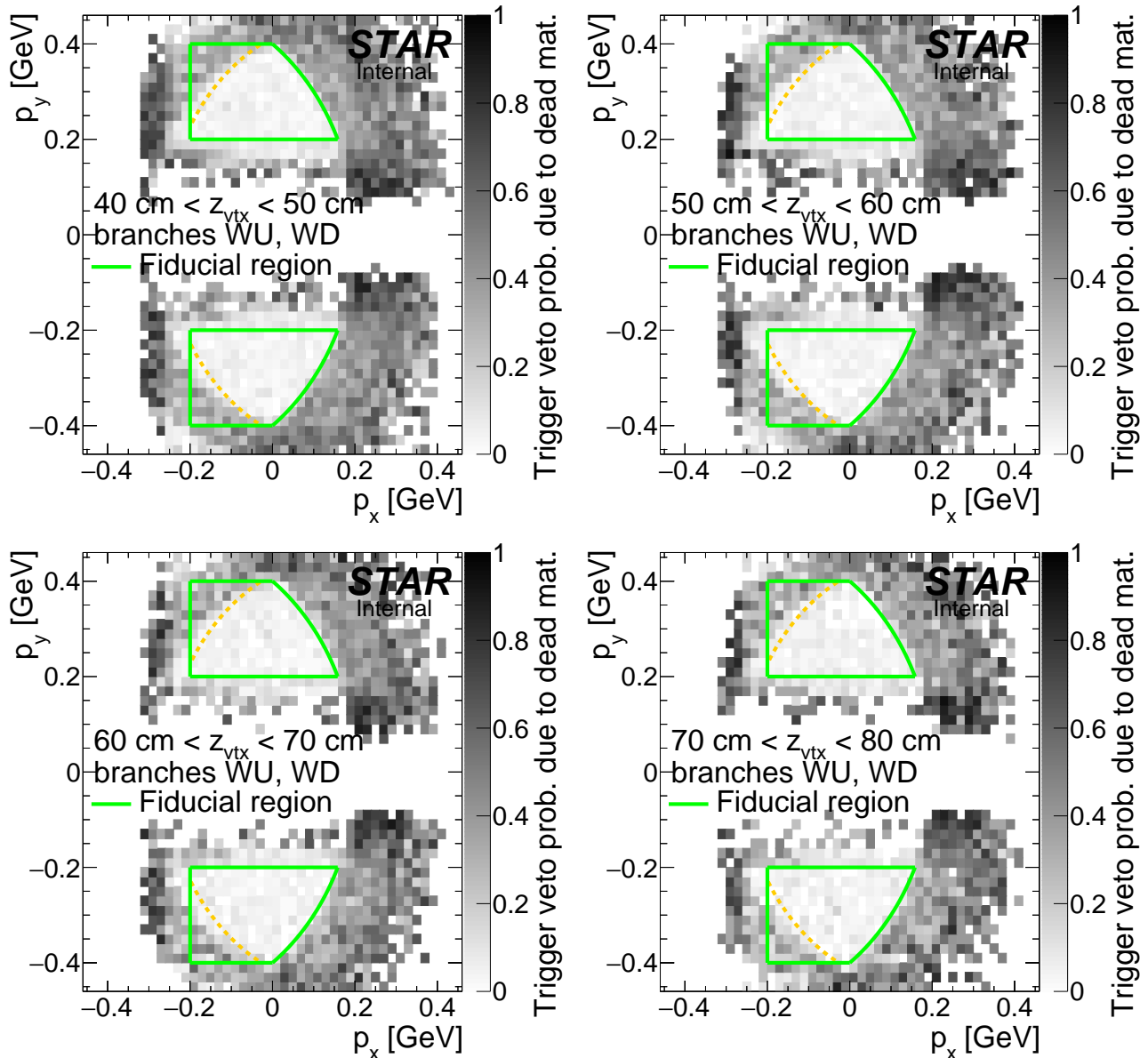


Figure D.4: Probability of ET&IT trigger veto due to forward proton interaction with dead material on the west side. Results were obtained from forward proton MC simulation embedded into zero-bias data. Each plot corresponds to z -vertex range given in the plot.







List of Figures

1.1	CEP represented in η - ϕ space.	5
1.2	Diagram of DIPE process.	5
2.1	Sketch of the trigger components used in definitions of diffractive triggers in run 15.	7
3.1	Primary vertex multiplicity. Red arrow marks bin with events with exactly one primary vertex (with track(s) matched with hit in TOF), which are used in physics analysis.	10
3.2	z -position of the primary vertex in single TOF vertex events. Red dashed line indicate range of longitudinal vertex position accepted in analysis.	10
3.3	Multiplicity of primary TPC tracks matched with hit in TOF for single TOF vertex events	11
3.4	Distribution of a distance in $\eta - \phi$ space between the BEMC cluster closest to primary TPC track (R_{\min})	11
3.5	Comparison of distribution of $N_{\text{hits}}^{\text{fit}}$, $N_{\text{hits}}^{\text{dE/dx}}$ and $N_{\text{hits}}^{\text{fit}}/N_{\text{hits}}^{\text{poss}}$ in the data and embedded MC	12
3.6	Comparison of distribution of track η and ϕ in the data and embedded MC	13
3.7	Local angles of global tracks in Roman Pots.	14
3.8	Correlation and difference of z -vertex position measured in Roman Pots and TPC.	14
3.9	Sample BBC-small and BBC-large response in zero-bias triggers.	15
3.10	Probability of false BBC-large signal (noise-induced).	16
3.11	NTofClusters.	16
3.12	Correlation between sum of corresponding momentum components (x in Fig. 3.12a and y in Fig. 3.12b) of Roman Pot proton tracks and TPC tracks.	17
3.13	MissingPt.	17
3.14	Correlation between $n\sigma^{\text{pair}}$ from TPC for $\pi^+\pi^-$, K^+K^- and $p\bar{p}$.	18
3.15	Correlation between m^2 from TOF and $n\sigma^{\text{pair}}$ from TPC for $\pi^+\pi^-$, K^+K^- and $p\bar{p}$.	18
3.16	Squared particle mass from TOF for candidates of given PID selected based on dE/dx in TPC.	18
3.17	Relation between $\pi^+\pi^-$ significance, efficiency and purity vs. thresholds in cuts C6, C7 and C8	19
3.18	Cut flow.	20
4.1	Overall efficiency of the online BBC-small and ZDC veto as a function of instantaneous luminosity.	21
4.2	Overall efficiency of the online BBC-small and ZDC veto, primary vertices limit (C1), BBC-large veto (C6) and TOF clusters limit (C7) as a function of instantaneous luminosity.	22
4.3	Comparison of m^2 from TOF between data and MC for exclusive $\pi^+\pi^-$, K^+K^- and $p\bar{p}$.	22
4.4	Sample RP track reconstruction efficiency in a single z -vertex bin.	23
4.5	Probability of simultaneous inefficiency of the RP track reconstruction calculated from the CEP MC embedded into zero-bias data.	
23		
5.1	Missing pT.	25
5.2	Graph illustrating the misidentification problem.	25
7.1		28
7.2		29
7.3		30
7.4		31
7.5	Cut flow.	32

A.1	Distribution of ADC vs. TAC counts (2D) and ADC conunts (1D) per BBC-small channel in abort gaps and colliding bunches.	33
A.2	Distribution of ADC vs. TAC counts (2D) and ADC conunts (1D) per BBC-large channel in abort gaps and colliding bunches.	39
C.1	Scheme of two central tracks with common vertex, hitting cells in TOF detector.	44
D.1	RP track acceptance, reconstruction and selection efficiency on the east (MC embedded into zero-bias data).	45
D.2	RP track acceptance, reconstruction and selection efficiency on the west (MC embedded into zero-bias data).	48
D.3	Probability of ET&IT trigger veto due to forward proton interaction with dead material on the east.	51
D.4	Probability of ET&IT trigger veto due to forward proton interaction with dead material on the west.	54

List of Tables

2.1	Central Diffraction physics triggers and control triggers involving Roman Pot detectors in run 15.	7
3.1	Offline ADC thresholds in BBC-large.	16

References

- [1] L. Adamczyk, L. Fulek, and R. Sikora, “Supplementary note on diffractive analyses of 2015 proton-proton data.” <https://drupal.star.bnl.gov/STAR/blog/rafals/supplementary-note-diffractive-analyses-2015-proton-proton-data>, January, 2019.
- [2] P. D. B. Collins, *An Introduction to Regge Theory and High-Energy Physics*. Cambridge Monographs on Mathematical Physics. Cambridge Univ. Press, Cambridge, UK, 2009.
<http://www-spires.fnal.gov/spires/find/books/www?cl=QC793.3.R4C695>.
- [3] S. Donnachie, H. G. Dosch, O. Nachtmann, and P. Landshoff, *Pomeron physics and QCD*, vol. 19. 2002.
- [4] V. Barone and E. Predazzi, *High-Energy Particle Diffraction*, vol. v.565 of *Texts and Monographs in Physics*. Springer-Verlag, Berlin Heidelberg, 2002.
<http://www-spires.fnal.gov/spires/find/books/www?cl=QC794.6.C6B37::2002>.
- [5] P. Lebiedowicz and A. Szczurek, “Exclusive $pp \rightarrow pp\pi^+\pi^-$ reaction: From the threshold to LHC,” *Phys. Rev.* **D81** (2010) 036003, [arXiv:0912.0190 \[hep-ph\]](https://arxiv.org/abs/0912.0190).
- [6] P. Lebiedowicz, O. Nachtmann, and A. Szczurek, “Central exclusive diffractive production of $\pi^+\pi^-$ continuum, scalar and tensor resonances in pp and $p\bar{p}$ scattering within tensor pomeron approach,” *Phys. Rev.* **D93** no. 5, (2016) 054015, [arXiv:1601.04537 \[hep-ph\]](https://arxiv.org/abs/1601.04537).
- [7] L. A. Harland-Lang, V. A. Khoze, and M. G. Ryskin, “Modelling exclusive meson pair production at hadron colliders,” *Eur. Phys. J.* **C74** (2014) 2848, [arXiv:1312.4553 \[hep-ph\]](https://arxiv.org/abs/1312.4553).
- [8] R. Fiore, L. Jenkovszky, and R. Schicker, “Resonance production in Pomeron–Pomeron collisions at the LHC,” *Eur. Phys. J.* **C76** no. 1, (2016) 38, [arXiv:1512.04977 \[hep-ph\]](https://arxiv.org/abs/1512.04977).
- [9] F. E. Close and A. Kirk, “A Glueball - q anti-q filter in central hadron production,” *Phys. Lett.* **B397** (1997) 333–338, [arXiv:hep-ph/9701222 \[hep-ph\]](https://arxiv.org/abs/hep-ph/9701222).
- [10] <https://online.star.bnl.gov/rp/pp200/>.
- [11] <https://online.star.bnl.gov/RunLogRun15/>.
- [12] <http://www.star.bnl.gov/protected/common/common2015/trigger2015/lumipp200GeV/>.
- [13] I. Alekseev and J. H. Lee, “Trigger Definitions for RP phase-II* for Run15.”
https://drupal.star.bnl.gov/STAR/system/files/trigger_updated_run15_v2.doc, December, 2014.
- [14] I. Alekseev, “Trigger with Roman Pots Phase II*.”
https://drupal.star.bnl.gov/STAR/system/files/trigger4RP2_v2.pdf, December, 2014.
- [15] R. Sikora, “Naming convention and layout of the Roman Pot Phase II* subsystem in the STAR experiment.” https://drupal.star.bnl.gov/STAR/system/files/RomanPotNomenclature_0.pdf, October, 2014.
- [16] <http://www.star.bnl.gov/public/comp/prod/DataSummary.html>.
- [17] <https://drupal.star.bnl.gov/STAR/event/2017/09/27/software-and-computing-meeting/revertexing-2015-rp-stream>.
- [18] L. Adamczyk. https://drupal.star.bnl.gov/STAR/system/files/talk_42.pdf, March, 2016.
- [19] <https://github.com/rafalsikora/CEP-STAR>.

- [20] R. A. Kycia, J. Chwastowski, R. Staszewski, and J. Turnau, “GenEx: A simple generator structure for exclusive processes in high energy collisions,” *Commun. Comput. Phys.* **24** no. 3, (2018) 860–884, arXiv:1411.6035 [hep-ph].